

The wake structure and thrust performance of a rigid low-aspect-ratio pitching panel

JAMES H. J. BUCHHOLZ AND ALEXANDER J. SMITS

Department of Mechanical and Aerospace Engineering, Princeton University, Princeton, NJ 08544, USA

(Received 21 July 2007 and in revised form 28 January 2008)

Thrust performance and wake structure were investigated for a rigid rectangular panel pitching about its leading edge in a free stream. For $Re_c = O(10^4)$, thrust coefficient was found to depend primarily on Strouhal number St and the aspect ratio of the panel AR . Propulsive efficiency was sensitive to aspect ratio only for AR less than 0.83; however, the magnitude of the peak efficiency of a given panel with variation in Strouhal number varied inversely with the amplitude to span ratio A/S , while the Strouhal number of optimum efficiency increased with increasing A/S . Peak efficiencies between 9% and 21% were measured. Wake structures corresponding to a subset of the thrust measurements were investigated using dye visualization and digital particle image velocimetry. In general, the wakes divided into two oblique jets; however, when operating at or near peak efficiency, the near wake in many cases represented a Kármán vortex street with the signs of the vortices reversed. The three-dimensional structure of the wakes was investigated in detail for $AR = 0.54$, $A/S = 0.31$ and $Re_c = 640$. Three distinct wake structures were observed with variation in Strouhal number. For approximately $0.20 < St < 0.25$, the main constituent of the wake was a horseshoe vortex shed by the tips and trailing edge of the panel. Streamwise variation in the circulation of the streamwise horseshoe legs was consistent with a spanwise shear layer bridging them. For $St > 0.25$, a reorganization of some of the spanwise vorticity yielded a bifurcating wake formed by trains of vortex rings connected to the tips of the horseshoes. For $St > 0.5$, an additional structure formed from a perturbation of the streamwise leg which caused a spanwise expansion. The wake model paradigm established here is robust with variation in Reynolds number and is consistent with structures observed for a wide variety of unsteady flows. Movies are available with the online version of the paper.

1. Introduction

Aquatic animals oscillate their flukes and fins to produce unsteady forces that manoeuvre and propel them through the water. The mechanisms of unsteady thrust production and the unsteady highly three-dimensional wake structures generated by these propulsors are currently not well-understood. However, work on two-dimensional oscillating foils has begun to elucidate factors that govern efficient thrust production, and the structure of unsteady wakes, as well as the relationship between wake structure and thrust performance. Under conditions of efficient propulsion, two-dimensional unsteady propulsors are known to generate two spanwise vortices per oscillation which are arranged into a staggered array resembling a Kármán vortex street, but with the signs of the vorticity reversed such as to increase the momentum flux in the wake over that in the free stream. Triantafyllou, Triantafyllou

& Grosenbaugh (1993) have referred to this pattern as a reverse Kármán vortex street and proposed the Strouhal number as the appropriate non-dimensional frequency governing wake patterns and thrust production by high-aspect-ratio unsteady foils:

$$St = \frac{fA}{U}. \quad (1.1)$$

Here, A is the wake width (often approximated by the peak-to-peak excursion of the trailing edge, which is the convention used here), f is the dimensional frequency of oscillation, and U is the free stream or relative translational speed of the fluid. The optimal range $0.25 \lesssim St \lesssim 0.35$ was predicted by a two-dimensional linear stability analysis on an experimentally measured mean wake profile under the assumption that forcing at the most unstable mode would result in the formation of the desired wake structure with minimum energy input, and therefore maximum efficiency. They supported their conclusion with experimental data and observations of the swimming gaits of a variety of aquatic animals.

Anderson *et al.* (1998) conducted a detailed parametric study of the thrust performance and wake structure of a pitching and heaving NACA 0012 airfoil and compared their measurements with the predictions of linear and nonlinear analytical models. Although, for a given set of kinematic parameters, the models predicted a single peak in efficiency within the range $0.1 < St < 0.2$, in several cases, the experimental data revealed a second peak within the range $0.3 < St < 0.4$, which was attributed to the wake dynamics described above. This second peak was regarded as more relevant to propulsors since the thrust coefficient was significantly higher than at the first optimum. Efficiencies as high as 87% were reported.

Efficient propulsion is frequently commensurate with the generation of leading-edge vortices which are shed at an appropriate phase to coalesce with vortices shed by the trailing edge, forming a reverse Kármán street (Oshima & Natsume 1980; Oshima & Oshima 1980; Freymuth 1988; Ohmi *et al.* 1990, 1991; Anderson *et al.* 1998). Under suboptimal conditions, the leading- and trailing-edge vortices fail to combine, forming four vortices per oscillation. The pattern has also been observed under conditions of drag (Koochesfahani 1989). These shedding patterns are similar to those produced by a vibrating circular cylinder, as observed by Williamson & Roshko (1988), which they called 2-S (two single vortices) in the case of two vortices generated per oscillation, and 2-P (two pairs) when four vortices were shed. Other patterns were also observed.

Gharib, Rambod & Shariff (1998) proposed an alternative paradigm to predict optimal performance of unsteady biological propulsors based on the generation of vortex rings using a piston and cylinder. They identified the formation number $n = L/D$ (L = piston stroke, D = diameter) such that for $n \approx 4$ both the vortex ring circulation and the time-averaged force were maximized. Further advancement of the piston resulted in the formation of a jet trailing the vortex ring. The formation number has been generalized to predict the generation of vortex rings through temporally varying orifices (Dabiri & Gharib 2005) and the optimal oscillatory motion of a finite-aspect-ratio plate in a quiescent fluid (Milano & Gharib 2005).

While it has been proposed that the wakes generated by the fins of swimming fish are composed of vortex rings (Drucker & Lauder 1999), yielding vortex patterns that can sometimes resemble the planar distributions produced by two-dimensional oscillating fins on planes parallel to the transverse motion, neither the formation of vortex rings, nor of planar vortex streets captures the complexity of the vortex interactions in the wakes of real finite-aspect-ratio biological propulsors. However,

some progress has been made in understanding the wake topology and performance characteristics of a variety of finite-aspect-ratio geometries.

Jiménez *et al.* (2003) and Buchholz *et al.* (2003) investigated the wake structures produced by very low aspect ratio ($AR = 0.27$) flexible panels actuated to approximate streamwise travelling waves. On the symmetry plane, a vortex was shed into the wake near the peak displacement of the trailing edge, followed by the shedding of a shear layer as the trailing edge swept across the wake. The shear layer rolled up into a discrete vortex, forming a transversely oriented counter-rotating vortex pair with the subsequent vortex in the following half-cycle. The vortex pairs formed a bifurcating wake. Similar wake development was observed by Tytell & Lauder (2004) in the wakes of American eels (*Anguilla rostrata*) swimming at the bottom of a water channel.

A three-dimensional wake model for a pitching and heaving wing of aspect ratio 3 was proposed by von Ellenrieder, Parker & Soria (2003) based on the visualization of dye injected from the surface of the wing. The model, valid for $0.2 < St < 0.4$ and chord Reynolds number $Re_C = UC/\nu = 164$, (U = free-stream velocity, C = chord length and ν = kinematic viscosity) consisted of two merged, closed vortex loops shed in each half-cycle, forming a zigzag chain, sometimes with additional appendages. Guglielmini (2004) simulated this experiment for Strouhal numbers of 0.175 and 0.35. Her computations at $St = 0.175$ revealed a chain of simple vortex rings of alternating sign, but at $St = 0.35$ the wake was found to divide into two chains of vortical structures with an appearance very different from that observed in the experiments by von Ellenrieder *et al.* (2003).

Dong *et al.* (2005) computed the wake structure and thrust performance of pitching and heaving ellipsoidal wings at $100 \leq Re_C \leq 400$, and aspect ratios varying from a circular planform to a two-dimensional foil. Increasing Reynolds number from 100 to 400 resulted in approximately a factor of two increase in propulsive efficiency. A bifurcating wake was observed for $0.3 \leq St \leq 1.2$ with transversely tilted vortex rings apparent in each branch of the wake. At infinite aspect ratio, a reverse Kármán vortex street was observed. Although thrust performance was found to be sensitive to Reynolds number in this range, the qualitative wake topology was quite robust.

In an earlier stage of the present work, Buchholz & Smits (2006) visualized wakes produced by a rigid panel of aspect ratio 0.54, pitching about its leading edge at $Re_C = 640$. At low Strouhal number ($St = 0.23$), a chain of structures was observed that was similar in appearance to the low-Strouhal-number wake produced by Guglielmini (2004). With increasing Strouhal number, the wake bifurcated, producing patterns similar to those of Guglielmini (2004) and Dong *et al.* (2005).

Clark & Smits (2006) investigated the wake structure and performance of an oscillating fin with elliptical planform. The fin was articulated with a streamwise travelling wave, increasing in amplitude in the spanwise direction. With relatively modest optimization of the kinematics, propulsive efficiencies of approximately 50% were achieved for $Re_C = O(10^4)$. From their measurements and observations, they inferred a distribution of bound vorticity strongly weighted toward the tip, which yields a wake structure composed of interconnected vortex loops with a corresponding distribution of circulation. Despite significant differences in geometry and kinematics, the topology of the wake is consistent with the model proposed by Buchholz & Smits (2006). With increasing Strouhal number, the wake also bifurcates.

This paper extends the work of Buchholz & Smits (2006) in which dye visualization and DPIV were used to investigate the wake structure of a rigid rectangular panel of aspect ratio $AR = 0.54$ pitching about its leading edge. At $Re_C = 640$, three distinct wake patterns were observed with variation in Strouhal number. The simplest

Panel	AR	S (cm)	C (cm)
1	0.54	6.5	12.0
2	0.83	10.0	12.0
3	1.11	13.3	12.0
4	2.38	28.5	12.0

TABLE 1. Panel dimensions.

structure, associated with the lowest Strouhal-number range ($0.20 \lesssim St \lesssim 0.25$), was investigated in detail and a three-dimensional vortex skeleton model was proposed. In the present work, we investigate the effect of variation of other parameters that define this problem; Reynolds number, panel aspect ratio, and pitching amplitude (non-dimensionalized by panel chord or span), seeking to identify and quantify the parameters that govern wake structure and thrust performance. Thrust performance is measured for $Re_C = O(10^4)$, and corresponding wake patterns are observed. Then the three-dimensional structure of the wakes at $Re_C = 640$ are re-visited, and the wake model of Buchholz & Smits (2006) is used to develop and understand vortex skeleton models for $St = 0.43$ and 0.64 . It is observed that features of these models are highly robust, and comparisons are made to the pitching panel wakes at $Re_C = O(10^4)$ and to other unsteady wakes summarized above.

2. Experimental apparatus and procedures

2.1. Experimental geometry

Experiments were conducted using four clear acrylic rectangular panels with aspect ratios $AR = S/C$ ($S = \text{span}$, $C = \text{chord}$) between 0.54 and 2.38 (table 1). Each panel had a thickness of 2.5 mm and $C = 120$ mm. For $AR = 2.38$ (panel 4 in table 1), the panel spanned the depth of the water to within 5 mm of the stationary top and bottom surfaces of the water tunnel and so its behaviour is expected to represent an aspect ratio greater than its physical dimensions produce. However, the aspect ratio is lower than that of nominally two-dimensional geometries observed in the literature (for example, Koochesfahani (1989) used $AR \approx 5$, and Anderson *et al.* (1998) used $AR = 6$), which employ endwalls that are fixed to and move with the foil.

The panel was supported by a stationary, symmetric airfoil fairing based on a NACA 0012-64 airfoil, as shown in figure 1(a). The fairing, with chord length $c = 50.8$ mm was truncated to allow the insertion of a 4.76 mm diameter stainless steel shaft, the *pitching shaft*, along the span of the fairing at $0.8c$. The leading edge of the panel was mounted to the pitching shaft (figure 1). For the low-aspect-ratio panels (panels 1 to 3), tapered trailing edge segments were mounted above and below the panel. On each side of the fairing, a series of 0.79 mm diameter spanwise holes spaced on 2.4 mm centres provided a means for dye injection from two separate cavities within the fairing. The fairing was made from ASTM 6061 aluminium for high stiffness and thermal conductivity (to help keep the dye in thermal equilibrium with the surrounding water) and was anodized to prevent corrosion.

The panel was activated in a pitching motion using a four-bar linkage driven by a d.c. servomotor as described in Buchholz & Smits (2006). The crank radius of the linkage allowed adjustment to control accurately the pitching amplitude of the panel, A , defined as the peak-to-peak excursion of the trailing edge. Thrust measurements

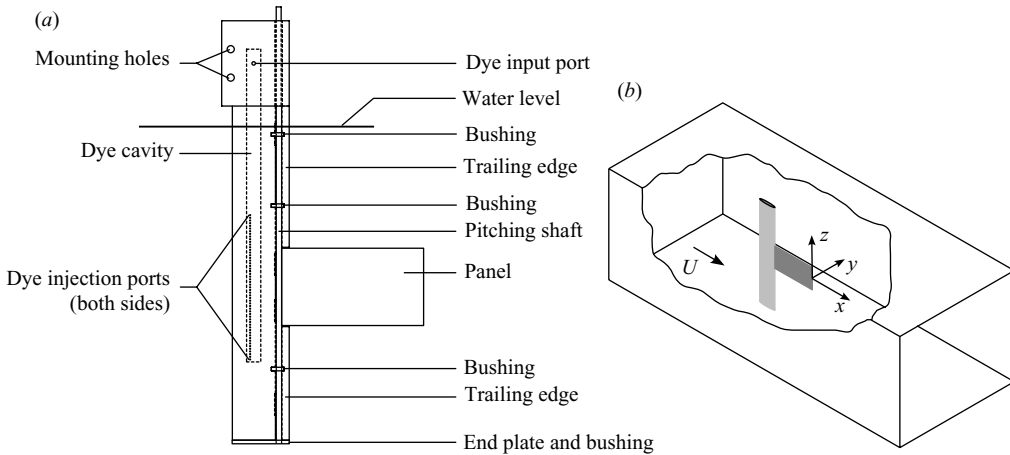


FIGURE 1. (a) The fairing and panel assembly. (b) Orientation in the water channel and coordinate system definition.

were facilitated by mounting the mechanism on a chassis supported by an air bearing sled (Daedalon Corporation) consisting of a pair of air tracks and 0.91 m long gliders.

The fairing and panel assembly was mounted vertically in a water channel of width 0.46 m and depth 0.29 m, with the centre of the panel positioned half-way between the top and bottom. Figure 1(b) shows the configuration and defines a coordinate system with the origin located on the symmetry plane (mid-span height) at the trailing edge of the panel, with the panel aligned parallel to the free stream. Two 12 mm thick, clear acrylic plates form a top wall, constraining the water surface over a 1.22 m streamwise extent centred about the fairing. The plates prevent the formation of surface waves near the panel and ensure undistorted observation of the flow, necessary for optical flow interrogation methods.

Flow conditioning in the water channel was achieved using a honeycomb flow straightener, three screens and a 5:1 contraction upstream of the test section. Low-Reynolds-number ($Re_c = 640$) wake investigations were conducted with a free-stream velocity U of 0.0053 m s^{-1} , while moderate-Reynolds-number ($Re_c = O(10^4)$) wake visualizations and thrust performance measurements were obtained at free-stream velocities between 0.029 and 0.285 m s^{-1} . Mean flow velocity and flow quality were assessed by imaging time lines produced by a vertical pulsed hydrogen bubble wire mounted upstream of the fairing, and using digital particle image velocimetry (DPIV). Typical streamwise turbulence intensities were 14 % in the low-Reynolds-number experiments, and 6 % in the moderate-Reynolds-number experiments – at such low flow velocities, it is difficult to achieve high flow quality. The mean flow velocity varied approximately 10 % across the region of the flow where measurements were made.

Because of the complexity of the flow field, flow visualization was used extensively to develop a qualitative understanding of the evolution of the wake structure. DPIV was used to validate observations made with flow visualization, to quantify aspects of these observations, and to provide insight into the generation of vorticity on the surface of the panel. Thrust performance was assessed by measuring mean thrust with a strain gauge-based force balance system, and hydrodynamic efficiency was determined with additional measurements of power imparted to the fluid by the panel.

2.2. Flow diagnostics

Three methods were used to illuminate dye patterns produced by the pitching panel: white halogen light, a laser scanning apparatus (developed by Delo, Kelso & Smits 2004) capable of illuminating 20 successive parallel planes, and a single laser sheet formed using an optical fibre delivery system with a Powell lens (Oz Optics). Photographs presented here were taken using the first two methods. Colour video and photographic data were obtained using Canon Mini-DV video cameras (NTSC) and a Sony DSC-V1 5.0 megapixel digital still camera. The still photographs were synchronized to the panel motion using the index channel of the encoder on the pitching shaft, which activated the camera shutter through a modified Sony RM-VD1 wired remote control. A Redlake HG-LE 8-bit monochrome CCD camera was used to acquire images in transverse (y, z)-planes illuminated by the laser-scanning drum, as described in Buchholz & Smits (2006).

The objective of dye visualization was to infer from the distribution of dye, the distribution and structure of vorticity in the wake, and, in particular, to identify concentrations of vorticity that are important to the evolution of the wake and the dynamics of unsteady thrust production. In this regard, dye visualization has a number of caveats that must be considered when interpreting the data (Lim 2000). In particular, the Schmidt number $Sc = \nu/\kappa = O(10^3)$ (ν = kinematic viscosity, κ = diffusivity of the dye). Therefore in non-turbulent flows, dye patterns can only effectively mark the vorticity in the early stages of evolution. Furthermore, the dye pattern is a spatially integrated representation of the flow, and therefore depends on the location at which the dye is introduced. Dye was injected from the two arrays of holes in the fairing. Fluorescein (Sigma-Aldrich 166308) was injected from the array on the left-hand side ($y < 0$), and sulforhodamine B (Sigma-Aldrich 230162) was injected from the right-hand side ($y > 0$) so that the origin of structures observed in the wakes could be inferred from the colour of the dye patterns. Both dyes had concentrations of 0.050 g l^{-1} .

Two dimensional velocity fields were obtained using DPIV for selected planes at discrete phases of the pitching cycle. DPIV data were acquired using the Lavisision Flowmaster 2 system with a New Wave Research Gemini double-pulse YAG laser ($120 \text{ mJ pulse}^{-1}$) and a Roper Scientific Megaplus ES-4.0 12-bit monochrome interline transfer CCD camera with 2048×2048 pixel resolution. The camera and laser were synchronized by a PC-based system containing a Lavisision programmable timing unit controlled using Lavisision's Davis 6 software. The flow was seeded using $14 \mu\text{m}$ diameter silver-coated hollow glass spheres with a true density of 1.7 g cm^{-3} (Potters Industries CONDUCT-O-FIL[®] SH400S33).

Two-dimensional discretely sampled velocity fields were computed by conducting local spatial cross-correlations, using software developed by Jiménez (2002), between the two images on corresponding 64×64 and subsequently 32×32 pixel windows with 50% overlap, to produce $128 \times 128 = 16384$ vectors. Sub-pixel accuracy was achieved using a 5×5 pixel Gaussian interpolant.

The velocity fields were obtained with two camera and laser sheet orientations. Top view images were acquired with a horizontal laser sheet positioned on the symmetry plane of the panel and the camera imaging from above the water channel. Upstream-looking images were acquired with the laser sheet oriented vertically at the desired streamwise location, and a 45° mirror was placed approximately 1 m downstream of the panel trailing edge so that images could be acquired with the same camera orientation. A transformation was applied to data acquired using the mirror to account for the reversed y -coordinate imaged by the camera.

The component of vorticity normal to the image plane was computed for each interior point (i, j) in the discrete velocity vector field. Vorticity at location (i, j) was determined by computing the circulation about a closed contour formed by the 8 surrounding points using the trapezoidal rule (Raffel, Willert & Kompenhans 1998).

Circulation of vortices was computed and compared by integrating the vorticity distribution within an isocontour of low vorticity value. The DPIV data often contained multiple vortices, with their shapes distorted owing to the interactions between them. Therefore the regions (or contours) of integration had to be carefully chosen. Vorticity values with magnitudes below the contour threshold were set to zero, and a minimal rectangular subdomain was defined in which the vorticity values were integrated. In most cases, this method effectively isolated the structure of interest since neighbouring vortices were typically of opposite sign and were easily filtered using the thresholding technique.

Velocity gradients and three-dimensionality were significant in regions investigated using DPIV, and were therefore important sources of error. The estimated uncertainty in velocity measurements is approximately 3%, and the uncertainty in vorticity and circulation measurements is approximately 5%. Because of the close proximity of vortices of opposite sign in the flows investigated here, diffusion of vorticity results in annihilation, and therefore vortex circulations are time-dependent. This variation was minimized by computing circulations on only the structure generated at the current phase and the immediately preceding structure.

2.3. Thrust and efficiency measurements

Time-averaged thrust measurements were obtained using an Omega LCAE-600G strain-gauge-based force sensor. The sensor had a 600 g capacity with nominally 0.02% nonlinearity and full-scale output of 1 mV V^{-1} . Excitation was $\pm 5 \text{ VDC}$. The output signal was amplified using an Analog Devices AD623 instrumentation amplifier configured with a gain of 1000.

A lever amplified the force applied to the load cell by a factor of 8, to provide adequate sensitivity while providing a resonant frequency far enough from the forcing frequencies such that oscillations could be damped with a simple dashpot. The dashpot consisted of an open container filled with SAE 85W-140 oil and a paddle mounted to the chassis. The resonant frequency was 1.1 Hz, and the panel was oscillated at frequencies $f = 2.00 \text{ Hz}$, 1.50 Hz, 0.70 Hz and 0.50 Hz. The primary forcing frequencies were at f owing to a small imbalance in the driving mechanism, and at $2f$, the dominant frequency of thrust production. The system used to obtain thrust and efficiency measurements is discussed in more detail in Buchholz, Clark & Smits (2008).

Experimental control and data acquisition were achieved using a desktop computer equipped with a National Instruments data acquisition card. A solenoid valve, activated by the computer, controlled air flow into the air tracks from a central building compressed air supply. The valve was opened in 22 s intervals beginning with a 7 s delay, followed by 15 s of data acquisition. Thrust measurements, obtained in this way, were used to compute thrust coefficients:

$$C_T = \frac{T}{\frac{1}{2}\rho U^2 SC}, \quad (2.1)$$

where T is the time-averaged thrust.

The Froude efficiency is the ratio of thrust power output to the total power input by the propulsor:

$$\eta = \frac{TU}{P_{inp}}, \quad (2.2)$$

where T is the time-averaged thrust generated by the panel and P_{inp} is given by:

$$P_{inp} = \eta_w P_w - \eta_a P_a. \quad (2.3)$$

P_w and P_a are the power consumed by the motor when driving the panel in water and air, respectively. η_w and η_a are the motor efficiencies at the respective motor operating conditions. The first term in (2.3) is the total mechanical power produced by the motor, and the second term is the power dissipated in the mechanical mechanism owing to friction. The P_a measurements are acquired in sets of three measurements before and after data acquisition in the manner described later in this section.

Power input to the motor P_m ($= P_w$ or P_a) is obtained by measuring the voltages across the motor and a 2.00 Ω , 1% tolerance power resistor R_s in series with the motor:

$$P_m = I_m V_m = \frac{V_R}{R_s} V_m \quad (2.4)$$

where V_R and V_m are the voltages measured across the series resistor and motor, respectively. R-C filters ($RC = 0.015$ s) smoothed the noisy signal produced by the pulse-width-modulated motor controller. Motor efficiency curves were determined by measuring motor power in the same manner, while using the motor to lift calibrated weights with a pulley and string. Measured motor efficiencies varied between approximately 10% and 50%.

A procedure was established to acquire a data set consisting of a series of thrust and motor power measurements for a single panel and pitching amplitude throughout the desired Strouhal number range. The load cell was statically calibrated before and after acquisition of a data set. Baseline power measurements with the water channel empty (to determine P_a in (2.3)) were also taken in sets of three to five measurements of 15 s duration.

The water channel was filled, and thrust and power measurements were acquired at each Strouhal number in sets of six measurements, $n = 0, 1, 2, \dots, 5$. For $n = 0, 2, 4$, the panel is pitching, and thrust and power measurements were acquired. For $n = 1, 3, 5$, baseline force measurements were acquired with the panel stationary and aligned with the flow in order to compensate for drift in the sensor. The time-averaged thrust T was computed by taking the difference between the means of the thrust and baseline measurements. Uncertainties in the measured quantities are defined as the standard error of the mean $\bar{\sigma} = \sigma/\sqrt{N}$, for each data point consisting of $N = 3$ measurements, where σ is the sample standard deviation. The error bars in figures 2 to 9 reflect these uncertainties.

3. Thrust performance

Measurements of time-averaged thrust, power and propulsive efficiency were obtained while varying Strouhal number with the combinations of aspect ratio (AR) and amplitude (A/S or A/C) given in table 2 for $Re_C = O(10^4)$. The Strouhal number range was constrained by the speed of the water channel, the resonant frequency of the force balance, the magnitudes of the thrust and transverse forces produced, and the pitching amplitude.

		Panel:	1	2	3	4
		AR:	0.54	0.83	1.11	2.38
(i)	$A = 2.0 \text{ cm}$: $A/C = 0.17$	A/S :	0.31	0.20	0.15	0.070
(ii)	$A = 3.1 \text{ cm}$: $A/C = 0.26$	A/S :	0.48	0.31	0.23	0.11
(iii)	$A = 4.1 \text{ cm}$: $A/C = 0.34$	A/S :	0.63	0.41	0.31	0.14

TABLE 2. Combinations of geometric parameters for which thrust performance was investigated.

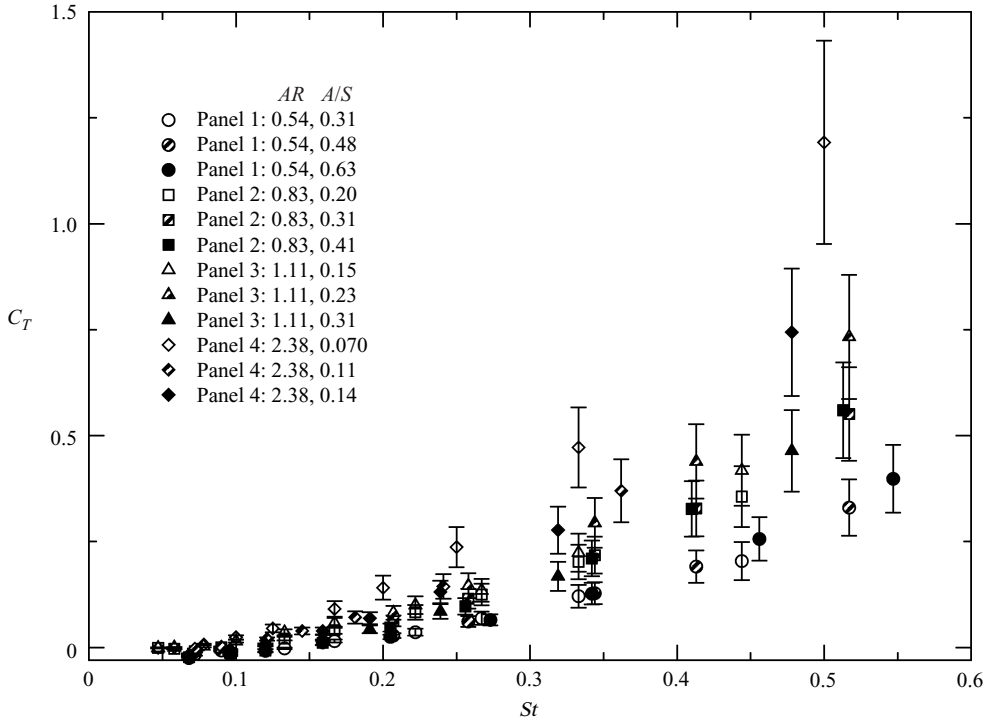


FIGURE 2. C_T for all four panels and all three amplitudes investigated ($St < 0.6$).

3.1. Thrust measurements

Figure 2 contains thrust coefficient data plotted as a function of Strouhal number for $St < 0.6$. The thrust coefficient increases monotonically with Strouhal number, with a similar shape for all four panels investigated. A principal result is that the C_T data collapse approximately onto curves of constant panel aspect ratio (AR). For constant Strouhal number, the corresponding point on each curve increases with AR . The values of C_T are low compared with other propulsors discussed in the literature. For panel 4, $C_T = 0.37$ at $St = 0.36$ and $A/S = 0.11$, and for panel 1, $C_T = 0.13$ at $St = 0.34$ and $A/S = 0.48$. In comparison, Anderson *et al.* (1998) measure C_T up to 0.75 at $St = 0.3$ for a pitching and heaving two-dimensional airfoil with varying forcing parameters ($Re_C = 40\,000$), and Clark & Smits (2006) measure C_T between approximately 1.3 and 2.0 for a three-dimensional articulated fin ($Re_C = 11\,000$). The low values in the present case are expected since this geometry was selected based on its simplicity rather than performance.

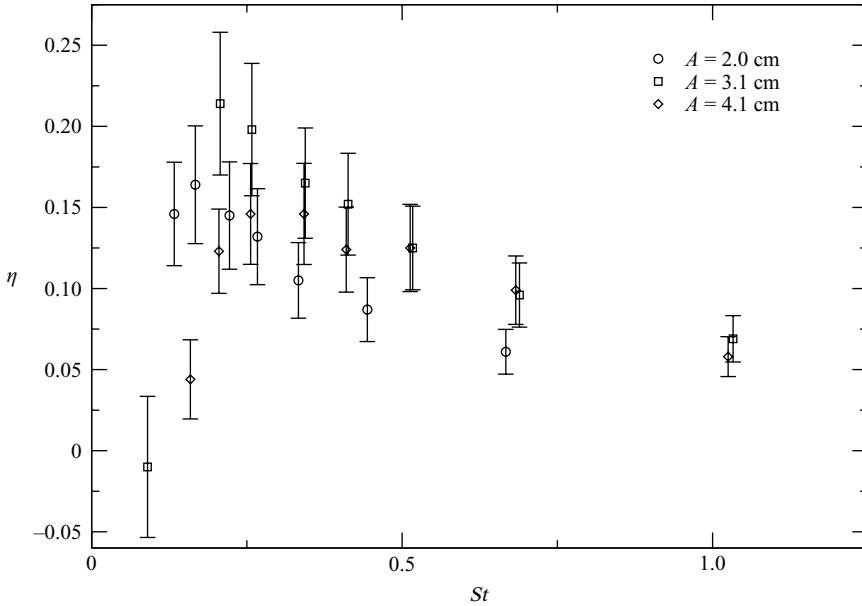


FIGURE 3. Propulsive efficiency of panel 2 ($AR = 0.83$).

Examination of the data of figure 2 in greater detail (not shown) reveals a secondary inverse relationship between C_T and pitching amplitude for panels 2 and 3 in the range $St \lesssim 0.25$, and for all of the data acquired for panel 4 (maximum $St = 1.0$). This is visible in figure 2 for panel 4.

3.2. Efficiency Measurements

Propulsive efficiencies for panels 2 and 4 are presented in figures 3 and 4. In this form, the relatively large uncertainties in the efficiencies obscure a detailed comparison of the effect of aspect ratio and pitching amplitude on the maximum efficiency and the Strouhal number at which it occurs. However, it is noted that optimal efficiencies for a given panel and pitching amplitude fall within the range $0.09 \lesssim \eta_{max} \lesssim 0.21$, and these optimal operating points occur for Strouhal numbers in the range $0.13 < St < 0.34$. Only four of the twelve cases (4 panels \times 3 amplitudes) have an optimal efficiency within the range of $0.25 \leq St \leq 0.35$ predicted by Triantafyllou *et al.* (1993) for two-dimensional foils. This is not surprising since most of the panels are of very low aspect ratio; however, none of the peak measurements of panel 4 fall into this range. The peak efficiencies for panel 4 are in the range $0.13 \leq St \leq 0.24$ which is similar to the optimal range of $0.1 \leq St \leq 0.2$ predicted by the analytical models used by Anderson *et al.* (1998) in which wake dynamics were not modelled.

Re-plotting the data in different forms, however, elucidates some trends. Figure 5 contains the peak efficiency values from each data set as a function of aspect ratio. Peak efficiencies of panel 1 ($AR = 0.54$) are distinctly lower than those for the higher-aspect-ratio panels; however, for the higher-aspect-ratio panels ($AR = 0.83, 1.11, 2.38$), the peak efficiency does not appear to be sensitive to aspect ratio. In figure 6, the same peak efficiency values are plotted against A/S , revealing a weak inverse trend. Such a trend is not evident when efficiency is plotted against A/C , suggesting that A/S is a more appropriate non-dimensionalization of pitching amplitude.

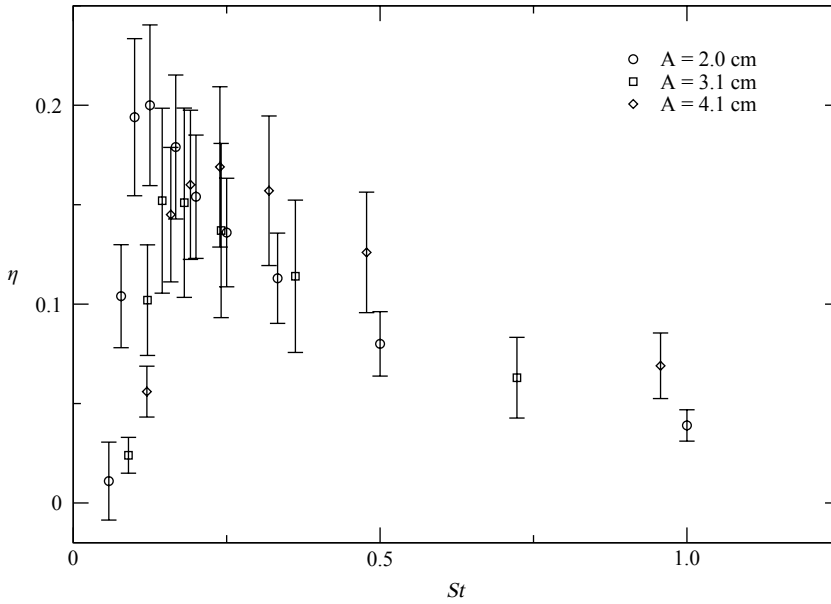


FIGURE 4. Propulsive efficiency of panel 4 ($AR = 2.38$).

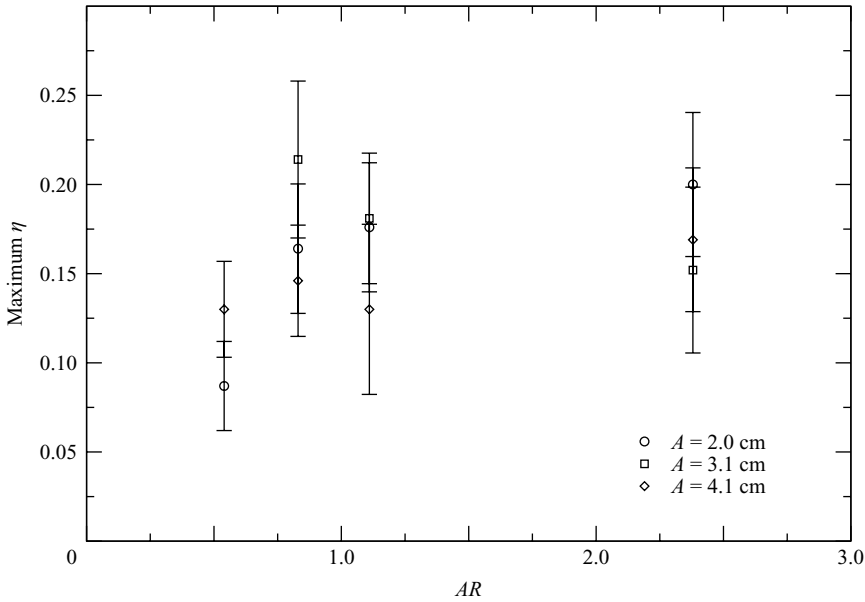
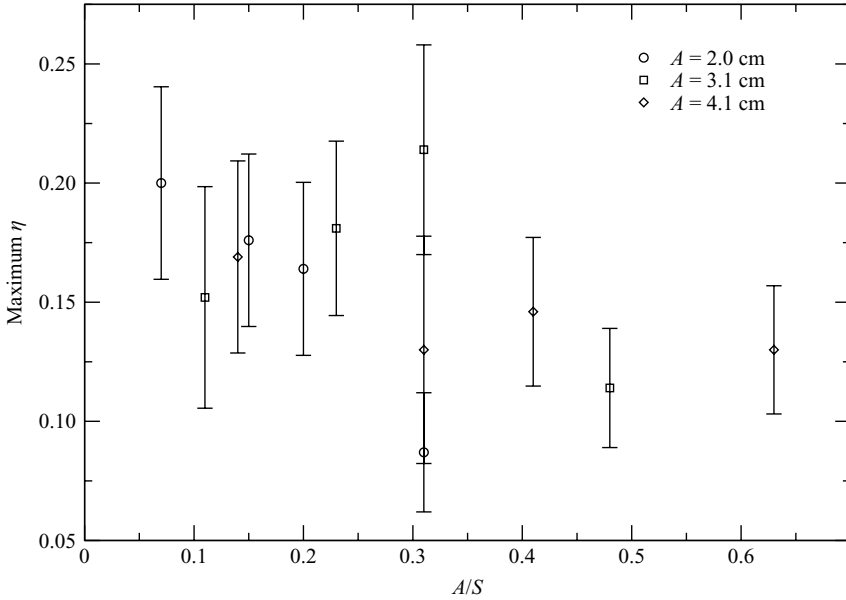
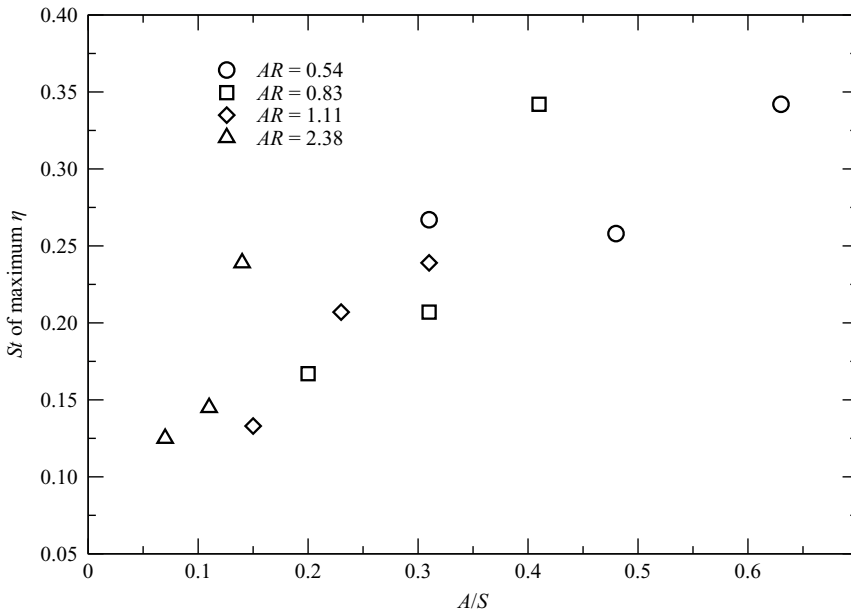


FIGURE 5. Dependence of propulsive efficiency on aspect ratio AR .

The Strouhal number of optimal efficiency is plotted in each case versus A/S in figure 7, revealing an inverse relationship between optimal Strouhal number and A/S . Plotting optimal Strouhal number against A/C does not yield a similar trend.

FIGURE 6. Dependence of optimal efficiency on A/S .FIGURE 7. Dependence of optimal Strouhal number on A/S .

3.3. The effect of Reynolds number on thrust performance

In all of the thrust performance experiments, the Strouhal number was varied by adjusting the free-stream velocity. Therefore it is necessary to assess the effect of the corresponding changes in Reynolds number. The influence of Reynolds number on thrust performance is also fundamentally of interest because it provides a measure of the generality of the thrust performance data presented here.

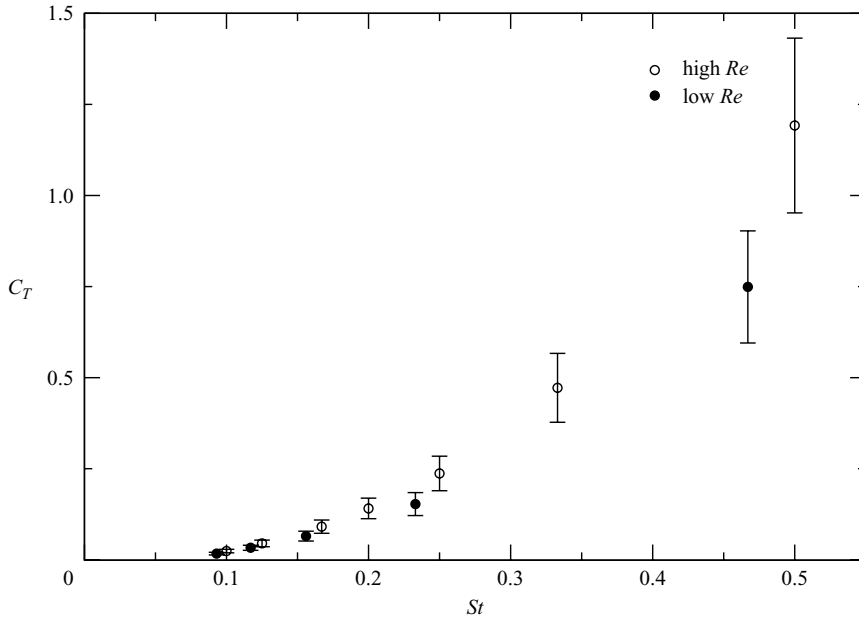


FIGURE 8. Effect of Reynolds number on thrust coefficient for panel 4 ($AR = 2.38$), $A = 2$ cm.

Reynolds-number effects were investigated by repeating portions of two data sets at reduced Reynolds number. Panel 2 with $A = 3.1$ cm was repeated for the range $0.14 \leq St \leq 0.72$ and $3200 \leq Re_C \leq 16\,200$, where the Strouhal-number range was approximately equal to that for the original data set at $9700 \leq Re_C \leq 32\,400$ (i.e. reduced by a factor of three). A portion of the data acquired from panel 4 with $A = 2.0$ cm was also repeated for $0.09 \leq St \leq 0.47$. This corresponded to $6000 \leq Re_C \leq 30\,000$ in the original data set and $3000 \leq Re_C \leq 15\,000$ in the reduced-Reynolds-number data set. The most significant disparities in C_T and η with reduction in Reynolds number were observed in the data of panel 4, therefore this case will be discussed here.

Figure 8 compares thrust coefficients produced by panel 4 for the two Reynolds number ranges. Pitching frequencies are constant within each data set, and consequently Re_C and St are inversely related. It would therefore be expected that Reynolds-number effects would be most significant for high values of St . Within the measurement uncertainty, there is not a clear distinction in the magnitude of the thrust coefficients measured in the two Reynolds number ranges. However, the mean values of propulsive efficiency, while obscured by large uncertainties, are approximately 5% lower in absolute efficiency (approximately 25% in relative magnitude) throughout most of the Strouhal number range examined. For panel 2, the low-Reynolds-number efficiency measurements are not consistently lower.

While these results incite caution in the interpretation of the efficiency data (particularly for panel 4), it should be noted that the peak efficiencies occur in the range $14\,400 \leq Re_C \leq 36\,000$. The vast majority of this Reynolds number range is greater than the values of Re_C included in the low-Reynolds-number data. Since Reynolds-number sensitivity is expected to decrease with increasing Re_C , the accuracy of the peak propulsive efficiency values measured in § 3.2, and the Strouhal numbers at which they occur, do not appear to be significantly affected by Reynolds number (figure 9).

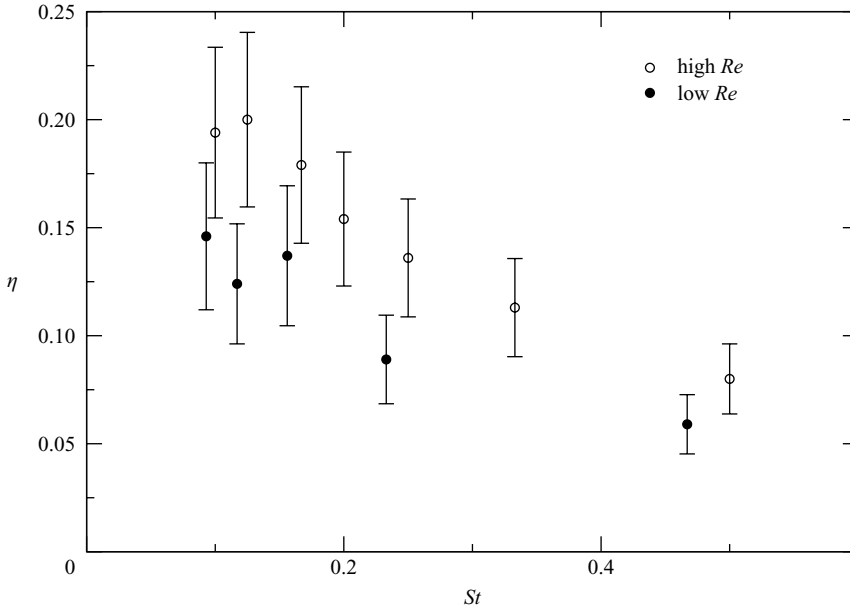


FIGURE 9. Effect of Reynolds number on propulsive efficiency for panel 4 ($AR = 2.38$), $A = 2.0$ cm.

4. Moderate-reynolds-number wakes

Dye visualization and DPIV were used to investigate the effects of experimental parameters on the distribution of vorticity in the wake and its evolution with downstream distance. Physical interpretations of the performance measurements of §3 are also sought through observation of the wake structure. As a benchmark, and to compare with investigations of two-dimensional foils, the wake of the high-aspect-ratio panel is investigated first.

4.1. The high-aspect-ratio panel (panel 4)

Dye visualization was used to investigate the wakes for a range of Strouhal numbers at pitching amplitudes of 2.0 cm ($A/C = 0.17$) and 3.1 cm ($A/C = 0.26$). This is a subset of the cases of table 2 for which thrust performance was measured.

A representative dye visualization sequence with varying Strouhal number is presented in figure 10 for $A = 3.1$ cm. In the top view perspective, rhodamine B (red) is injected from the upper side of the fairing, and fluorescein (green) is injected from the lower side. The evolution of wake structure with Strouhal number was found to be similar at $A = 2.0$ cm. Below the Strouhal number of maximum measured efficiency, dye visualization did not reveal the presence of any discrete vortices in the wake. However, for optimal forcing parameters, ($St = 0.13$ for $A = 2.0$ cm, and $St = 0.15$ to 0.18 for $A = 3.1$ cm), two vortices of opposite sign are shed in each pitching cycle, producing a wake with the appearance of a reverse Kármán vortex street (figures 10*b, c*). The vortices are connected by shear layers in which smaller spanwise vortices are visible (see, in particular, figure 10*c*).

With increasing Strouhal number, the streamwise spacing of the vortices decreases (figure 10*d*), and the wake ultimately becomes asymmetrical (figures 10*e, f*) with an appearance similar to that of the computations by Jones, Dohring & Platzer (1998).

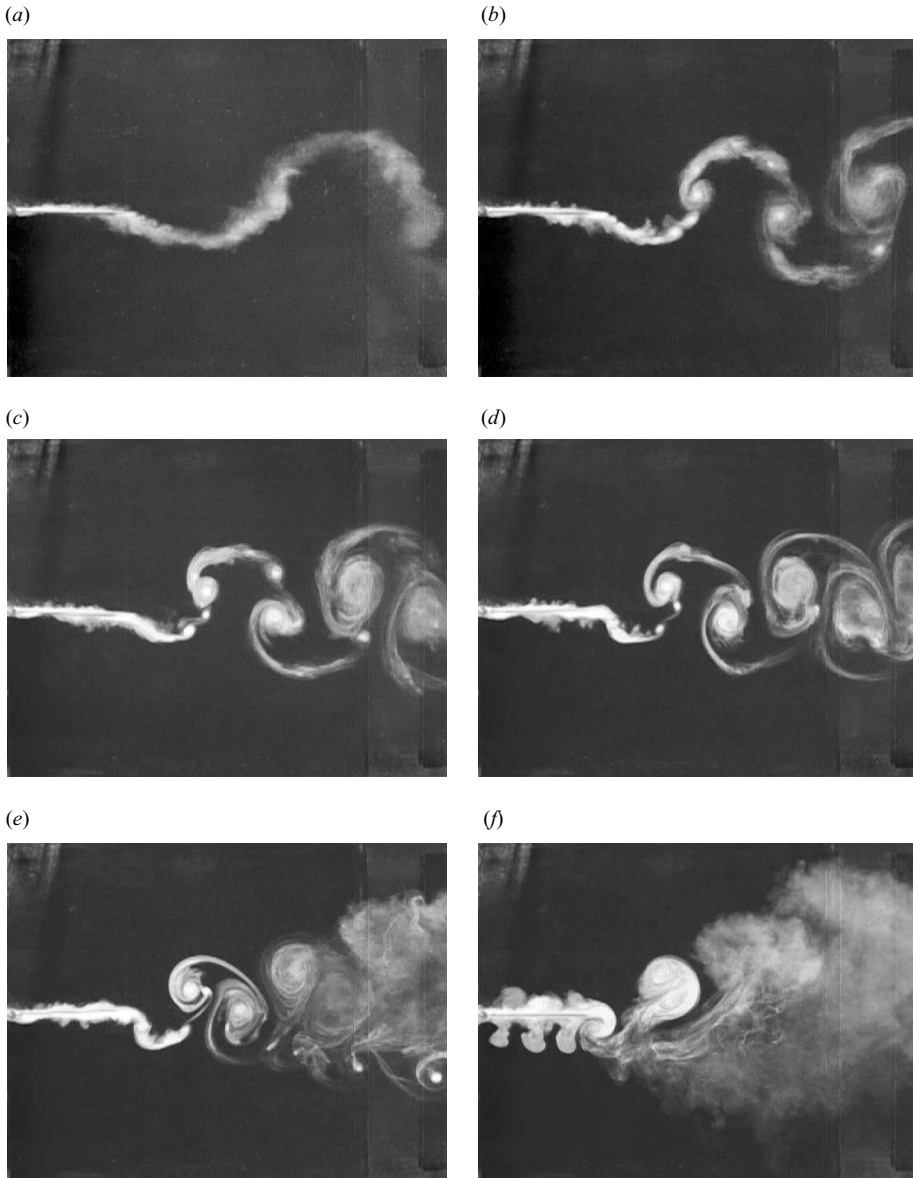


FIGURE 10. Dye visualization for the high-aspect-ratio panel, $A = 3.1$ cm ($A/C = 0.26$) corresponding to selected points in figure 4. Optimal efficiency measurements were obtained for $St = 0.15$ and 0.18 ($\eta = 0.15$, $Re_C = 18\,000$ and $14\,400$). (a) $St = 0.090$, (b) 0.15 , (c) 0.18 , (d) 0.24 , (e) 0.36 , (f) 0.72 .

The vortices in the asymmetrical wakes become turbulent within about one period. The pattern of dyed *mushrooms* observed along the panel in figure 10(f) are indicative of a periodic adverse pressure gradient on the panel and fairing. Reverse flow was not observed at any point, but the deceleration caused by the time-varying pressure gradient resulted in the injection of localized packets of dye due to the approximately constant volume flow rate of dye from the fairing. The mushroom shape results from the transverse momentum of the injected dye. These structures are weak compared to

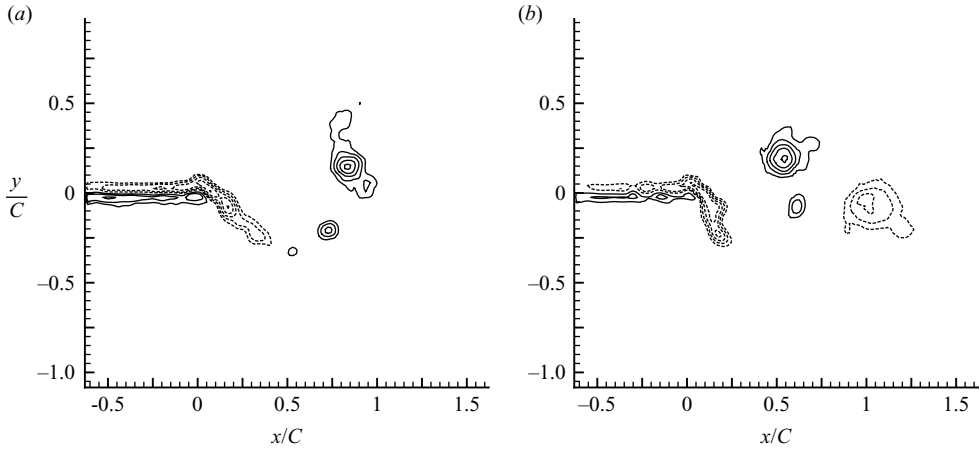


FIGURE 11. Phase-averaged isocontours of spanwise vorticity (30 realizations per average) in the wake of panel 4 with $A/C = 0.26$ ($A = 3$ cm) and (a) $St = 0.18$, $Re = 14\,400$, (b) $St = 0.36$, $Re_C = 7200$. Contour levels are $\pm n^2 \text{ s}^{-1}$, $n = 2, 3, 4, \dots, 10$. Dashed lines denote negative values.

those generated by the panel, and appear to be insignificant to the dynamics of the wake. At lower St , they are much less apparent.

DPIV was used to investigate the wake produced with $A/C = 0.26$ for $St = 0.18$ and $St = 0.36$. Figure 11 contains phase-averaged isocontours of spanwise vorticity for both cases at $\phi = 0^\circ$. At this phase, a shear layer extends from the trailing edge of the panel in each case. Much of the shear-layer vorticity ultimately rolls into a discrete vortex within a half pitching cycle, as the images indicate for the previously shed vortex of the opposite sign. In figure 11(a), two smaller discrete vortices form between the two shedding events, which were seen in figure 10(c). The final configuration is a staggered array of roughly axisymmetric vortices forming a reverse Kármán vortex street. DPIV data at $St = 0.36$ and $St = 0.72$ (not shown) yield a mean symmetric wake inconsistent with the flow-visualization observations in figures 10(e) and 10(f). The discrepancy implies the existence of more than one stable vortex pattern under these conditions with selection determined by either a finite asymmetry in the pitching motion or by conditions at the initiation of the pitching motion as observed by Jones *et al.* (1998).

4.2. Small-aspect-ratio panels

Dye injection was used to visualize the wakes of the small-aspect-ratio panels for each combination of parameters in which thrust was measured in §3. A subset of these cases was investigated in more detail using DPIV. Representative cases are presented here.

4.2.1. Panel 2: $AR = 0.83$, $A/S = 0.31$

Figure 12 contains flow visualization images for $AR = 0.83$, $A/S = 0.31$ ($A = 3.1$ cm) at four representative Strouhal numbers within the range investigated. Wake patterns are exhibited here that are broadly representative of all of the small-aspect-ratio cases investigated. Exceptions will be discussed subsequently.

Below approximately $St = 0.16$, the wake (when viewed from the top) has a sinusoidal appearance similar to that seen for panel 4 in figure 10(a). Figure 12(a) shows the wake at $St = 0.16$ where the dye pattern is beginning to evolve into an antisymmetric pattern composed of discrete structures that grows in the transverse direction with downstream distance from the panel. The maximum measured efficiency

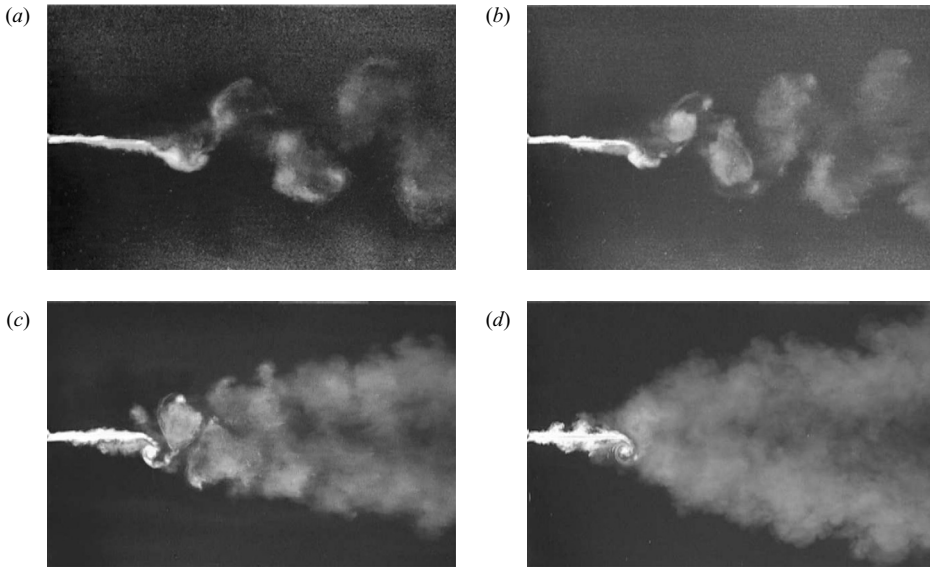


FIGURE 12. Dye visualization for panel 2: $AR = 0.83$, $A/S = 0.31$, $A/C = 0.26$, corresponding to selected points in figure 3. (a) $St = 0.16$, (b) 0.21, (c) 0.41, (d) 1.0. The maximum efficiency occurs at $St = 0.21$ ($\eta = 0.21$, $Re_C = 36\,000$).

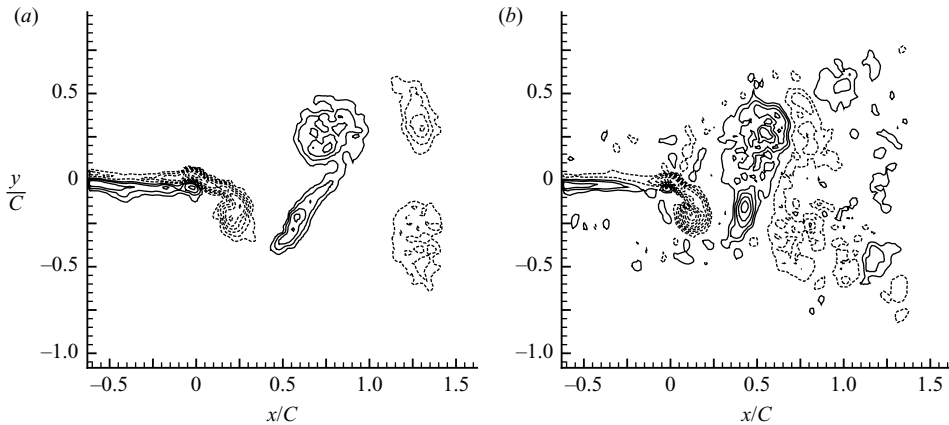


FIGURE 13. Isocontours of vorticity for panel 2, $A/S = 0.31$, $\phi = 0^\circ$, and (a) $St = 0.21$, $Re_C = 36\,000$, (b) $St = 0.41$, $Re_C = 18\,000$. Contour values are $\pm n^2 \text{ s}^{-1}$, $n = 2, 3, 4, \dots, 10$. Dashed lines denote negative values. Images are derived from 30 phase-averaged realizations.

occurs at $St = 0.21$ (figure 12b) where, in the top view, the near wake resembles a reverse Kármán vortex street. Further downstream, the structures spread in the transverse direction and lose their axisymmetric shape. This evolution is illustrated in movie 1 available with the online version of the paper. At $St = 0.41$, the spanwise vortices break down within a shorter distance from the trailing edge and divide, yielding a clearly bifurcating wake shown in figure 12(c) and movie 2. At $St = 1.0$, although the dye pattern indicates a single spanwise vortex shed in each half-cycle, the wake rapidly bifurcates into two oblique turbulent jet-like flows.

Figure 13 contains phase-averaged contours of spanwise vorticity in the symmetry plane at $St = 0.21$ and 0.41, for $\phi = 0^\circ$. By comparison with the panel 4 data of

figure 11, in each half-cycle, the shear layer following each discrete vortex appears to have much more significant circulation. It rolls into a separate discrete vortex and the two structures are convected downstream in separate branches of the wake. Although the vorticity contours at $St=0.41$ (figure 13*b*) appear much more complex than at $St=0.21$ (figure 13*a*), the fundamental topology is similar in both cases. In one pitching cycle, a counter-rotating vortex pair is formed in each branch of the wake. The transverse orientation of these spanwise pairs suggests a mechanism for the bifurcation of the wake, and thus produces some insight into the fundamental difference in behaviour between the wakes of panel 4, and the smaller-aspect-ratio panels.

4.2.2. Panel 1: $AR=0.54$, $A/S=0.31$

Panel 1 ($AR=0.54$) is the lowest-aspect-ratio panel investigated here, and it is the only one for which the reverse Kármán pattern was not observed for any combination of parameters examined. In addition, panel 1 consistently yielded the lowest peak efficiencies of all the panels for each pitching amplitude ($A=2.0$ cm, 3.1 cm, and 4.1 cm), as figure 5 indicates.

With $A=2.0$ cm ($A/S=0.31$), the maximum efficiency was measured at $St=0.27$. Top- and side-view flow visualization for this case is given in figure 14(*a*) where it is apparent that the wake is compressed in the spanwise extent immediately downstream of the trailing edge. In comparison, at $St=1.3$ (figure 14*b*) there is considerable spanwise ejection of fluid over approximately the last 25% of the chord, yielding a broad wake in the spanwise direction. This variation from spanwise compression to expansion with increasing Strouhal number is also apparent in the wakes of panels 2 and 3.

4.2.3. The significance of ratios A/S , AR , A/C

Section 3 indicated that the parameter A/S was important in governing the peak propulsive efficiency and the Strouhal number at which it occurred; however, there is considerable scatter. As table 2 shows, $A/S=0.31$ can be achieved for each of panels 1 to 3 for appropriate values of the pitching amplitude. We have already discussed figure 12(*b*), which shows the wake for panel 2 ($AR=0.83$) and $A/S=0.31$ under optimal propulsive conditions ($St=0.21$) where the reverse Kármán pattern is observed in the near wake. Likewise, figure 14(*b*) shows the wake for panel 1 ($AR=0.54$) and $A/S=0.31$ at its optimal $St=0.27$ in which the wake does not bear any resemblance to a reverse Kármán street. It may be argued that the lower aspect ratio in this case increases the interaction between the spanwise vorticity shed from the trailing edge and streamwise vorticity shed from the lateral edges of the panel, thus inhibiting organization of the spanwise vorticity. We might then expect that for panel 3 ($AR=1.11$) and $A/S=0.31$, the stability of the reverse Kármán structure would be even greater than for panel 2, as we have seen that this structure is quite robust for panel 4. However, as figure 15 shows, spanwise vorticity does not organize itself this way.

To maintain constant A/S with increasing AR , it is necessary to increase A/C (only two of the quantities A/S , A/C and AR may be varied independently). Therefore, as table 2 indicates, to maintain $A/S=0.31$, panels 1, 2, and 3 require A/C of 0.17, 0.26 and 0.34, respectively. In the case of panel 3, the large value of A/C has an adverse effect on thrust performance (possibly related to flow separation on the panel), and produces a more complicated wake structure in comparison with panel 2.

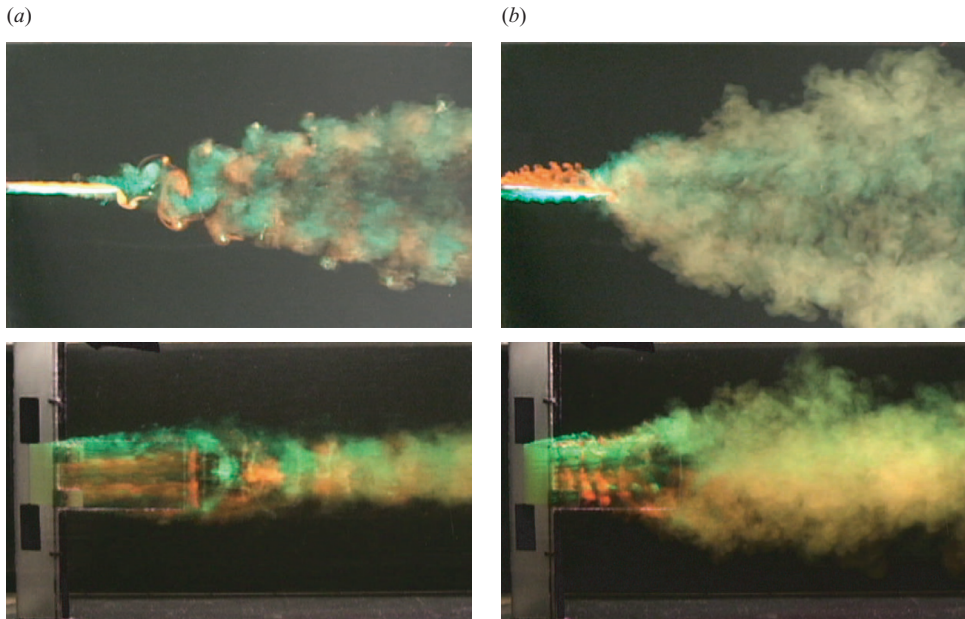


FIGURE 14. Dye visualization for panel 1: $AR = 0.54$, $A/S = 0.31$, $A/C = 0.17$. (a) $St = 0.27$, (b) 1.3. Maximum efficiency occurs at $St = 0.27$ ($\eta = 0.09$, $Re_C = 18\,000$).

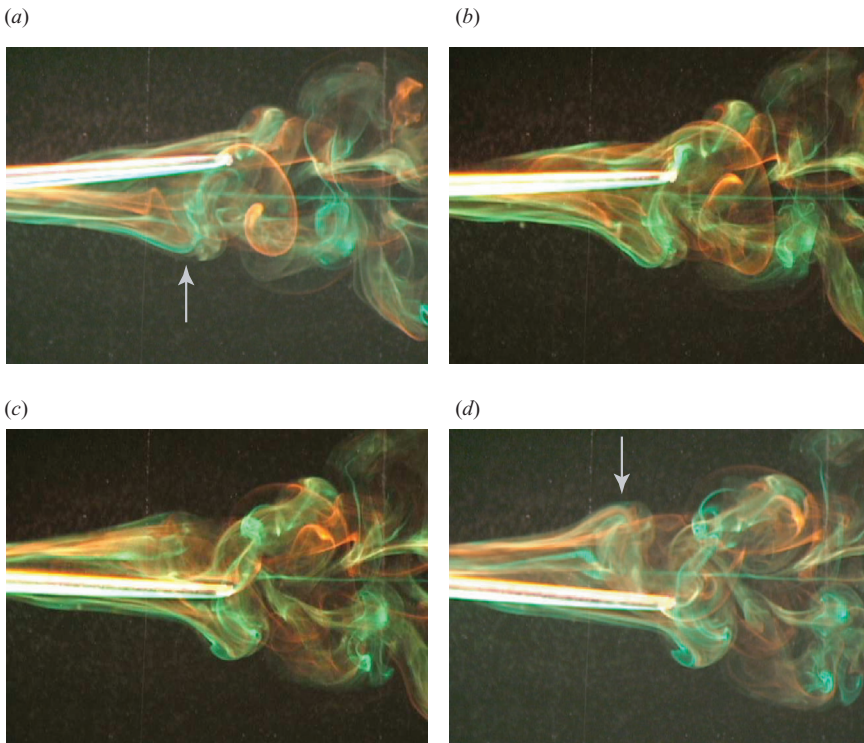


FIGURE 26. Top view of hairpin formation at $St = 0.64$, $Re_C = 640$. (a) $\phi \approx 90^\circ$, (b) 150° , (c) 210° , (d) 270° .

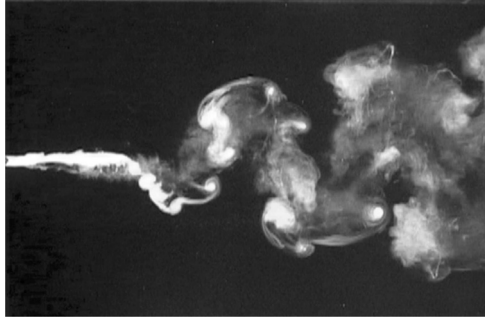


FIGURE 15. Wake structure produced by panel 3 ($AR=1.11$), $A=4.1$ cm ($A/S=0.31$, $A/C=0.34$) and $St=0.24$ (the optimal Strouhal number for this configuration). A complex pattern is formed in the wake.

While A/S has an important role in governing propulsive efficiency and wake structure for all of the cases investigated in this study, small values of AR and large values of A/C are observed to adversely affect propulsive efficiency, with commensurate changes in wake structure. It is proposed that for $A/S=0.31$, panel 2 has the aspect ratio which results in the optimal combination of A/C and AR . Of the three cases in which $A/S=0.31$, panel 2 has the greatest peak efficiency: $\eta_{max}=0.21$ compared with $\eta_{max}=0.09$ for panel 1 and $\eta_{max}=0.13$ for panel 3.

5. Low-Reynolds-number wakes

Flow-visualization and DPIV experiments were conducted at low Reynolds number ($Re_C=640$) to enable a detailed investigation of the vortical structure of the wake and its evolution. The wake was interrogated for $AR=0.54$ and $A/S=0.31$. With increasing Strouhal number, two transitions in wake structure were observed and previously reported in Buchholz & Smits (2006) for this configuration, which separate three notably different patterns in the wake.

The first and simplest structure is found for approximately $0.20 < St < 0.25$, and was studied in detail by Buchholz & Smits (2006) using dye visualization. Figure 16 contains dye-visualization images and spanwise vorticity contours for $St=0.23$. From the top, the wake has the appearance of a Kármán vortex street, whereas from the side it resembles a chain of linked vortex rings. Isocontours of positive vorticity (counterclockwise rotation) are indicated by solid lines while negative vorticity is indicated by dashed contours. A spanwise compression is noted beyond the trailing edge of the panel, similar to figure 14(a). The relevant features of this case will be briefly summarized here, and new quantitative results will be presented. The remainder of this section will address the more complex flows found at higher Strouhal numbers. For $St \gtrsim 0.25$, the wake divides, forming two separate trains of vortex structures similar in appearance to the small-aspect-ratio wakes presented in §4.2. Figure 17 shows illustrates this wake pattern with dye visualization and isocontours of vorticity. For Strouhal numbers greater than approximately 0.5, streamwise vorticity shed near the trailing edge develops a perturbation which evolves into a localized hairpin that convects outward in the spanwise direction under its own self-induction, making the wake appear much broader in the spanwise direction, as figure 18 shows for $St=0.64$.

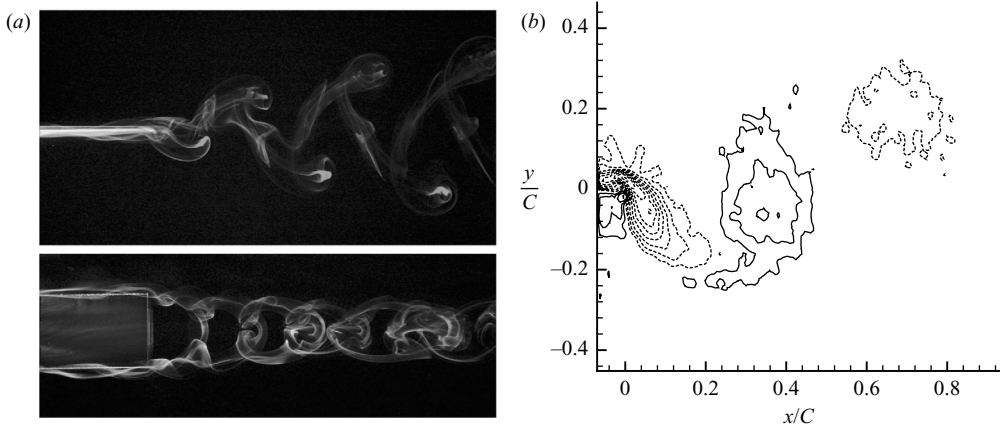


FIGURE 16. Dye visualization and isocontours of spanwise vorticity from DPIV data in the symmetry plane for $St=0.23$. Vorticity contour levels are $\pm(0.17n)^2 s^{-1}$, $n=2, 3, 4, \dots, 10$. Dashed lines denote negative values. (a) appears in Buchholz & Smits (2005, 2006); used with the permission of Cambridge University Press and the American Institute of Physics.

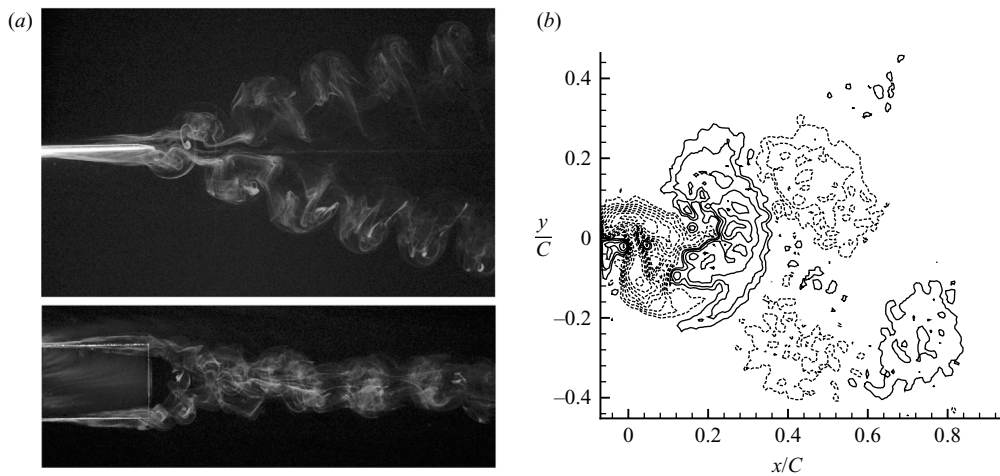


FIGURE 17. Dye visualization and isocontours of spanwise vorticity from DPIV data in the symmetry plane for $St=0.43$. Vorticity contour levels are $\pm(0.17n)^2 s^{-1}$, $n=2, 3, 4, \dots, 10$. Dashed lines denote negative values. (a) appears in Buchholz & Smits (2005, 2006); used with the permission of Cambridge University Press and the American Institute of Physics.

5.1. The vortex structure at $St=0.23$, $AR=0.54$, $A/S=0.31$

Twice per flapping cycle, vorticity shed from the three free edges of the panel forms a horseshoe vortex that is the main constituent of the wake. Figure 19 contains vortex skeleton depictions of a single horseshoe and the wake structure resulting from continuous generation of horseshoes. In these diagrams, the thickness of a vortex tube is intended to imply roughly the relative magnitude of its circulation, and the local directions of the vorticity vectors are indicated by the arrows.

Circulation varies along the legs of each horseshoe, reaching a maximum at the tip. This variation is attributed to spatial and temporal variations in the pressure distribution on the panel. Pressure gradients are the primary source of vorticity on

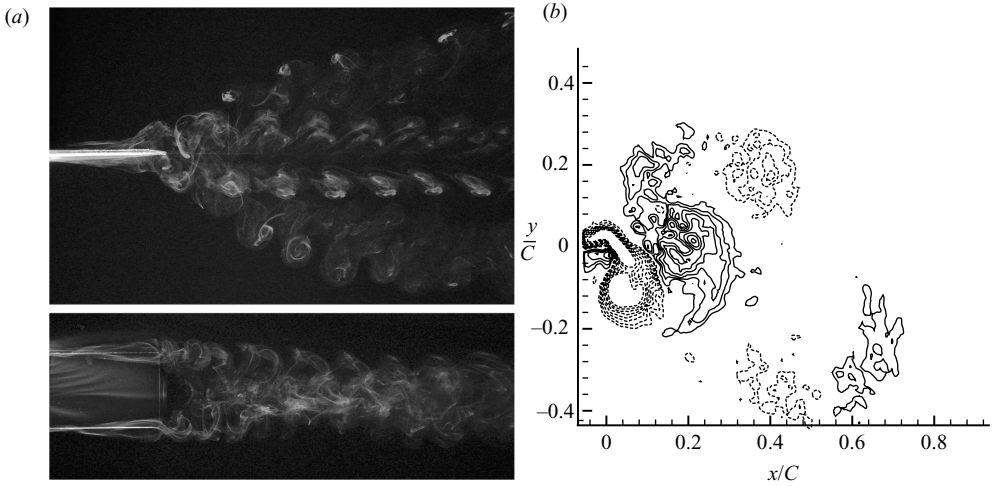


FIGURE 18. Dye visualization and isocontours of spanwise vorticity from DPIV data in the symmetry plane for $St=0.64$. Vorticity contour levels are $\pm(0.17n)^2 s^{-1}$, $n=3, 4, \dots, 10$. Dashed lines denote negative values. Part (a) of this figure appears in Buchholz & Smits (2005, 2006); used with the permission of Cambridge University Press, the American Institute of Physics, and the authors.

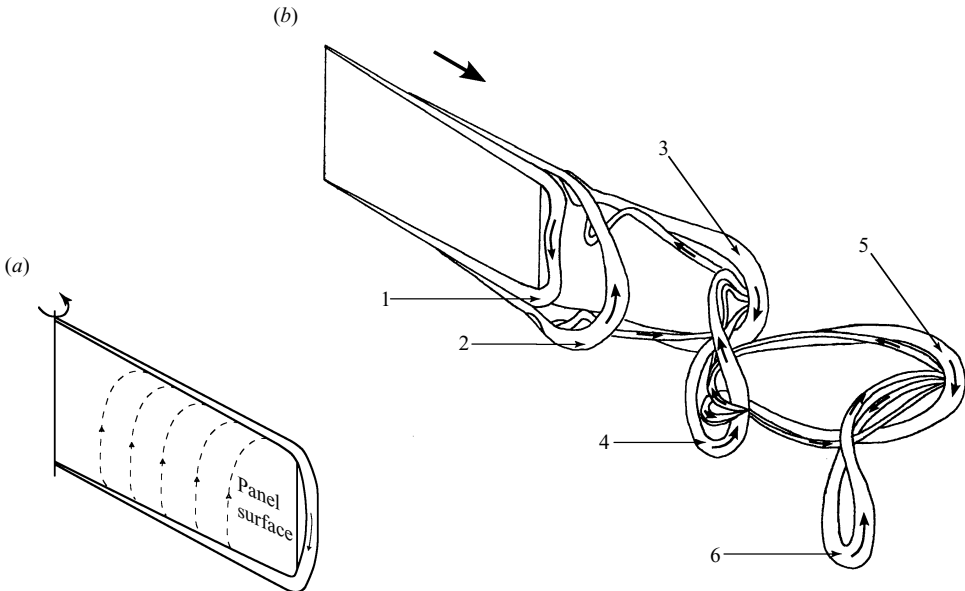


FIGURE 19. (a) A horseshoe vortex is shed twice per cycle at $St=0.23$, $Re_C=640$. Streamwise variation in circulation of streamwise legs is accompanied by a spanwise shear layer. The dashed lines depict vortex lines on the back of the panel. (b) A vortex skeleton model of the wake for $St=0.23$, $AR=0.54$, $A/S=0.31$ and $Re_C=640$. [A version of this figure appears in Buchholz & Smits (2006); used with the permission of Cambridge University Press.]

the panel (Lighthill (1963) and Wu & Wu (1996) address the generation of vorticity at a solid wall in detail), which vary periodically as the lift force alternates in sign through a pitching cycle. In addition, the pressure gradients are expected to vary in magnitude

with streamwise position as the transverse velocity of the panel increases linearly from the leading edge (where it is zero) to the trailing edge. The streamwise variation is accompanied by a spanwise shear layer shown in figure 19(a) which is the net circulation per unit chordwise length of the boundary layers on both sides of the panel. Hence, each horseshoe is not an open loop; it is rather a collection of closed-loop vortices bound together at the tip, and branching out from the legs in a distribution along the length of the structure to form the spanwise shear layer. Thus, for a given streamwise interval, the change in circulation of the (streamwise) legs of the horseshoe must be equal to the circulation of the (spanwise) shear layer over that interval.

The wake is constructed of a series of horseshoes, alternating in sense. The structures are numbered (figure 19b) beginning with the one being shed at the current phase, incrementing in reverse chronological order. Interactions between consecutive horseshoes are dominated by the most recently created structure owing to the streamwise staggering of the structures and their streamwise variation in circulation. The tip region of each horseshoe entrains a portion of the legs of the preceding horseshoe, and likewise has a portion of its legs entrained by the following horseshoe, in opposite-sign interactions. However, only a localized section of each leg is entrained. Further upstream, the streamwise vortices are ultimately entrained by a horseshoe of the same sign, created a full period later. The model is an idealization; the interactions are not precisely repeatable between experiments and varying degrees of entrainment occur.

Figure 20 contains isocontours of streamwise vorticity at four streamwise locations on the panel and in the wake. In figures 20(a) and 20(b), regions of positive and negative streamwise vorticity are apparent along the chord of the panel owing to the overlap between consecutive structures depicted in figure 19. The inner vortices are being generated at the current phase whereas the outer vortices were generated during the preceding half-cycle. Horseshoes 1 and 2 are both present in figures 20(a) and 20(b). Horseshoe 2 extends into the wake and is evident in all subsequent planes. Horseshoe 3 appears above the lowest contour threshold at $x/C = 0.33$ in figure 20(d).

The distributions of vorticity shown in figures 19 and 20 also explain the global dynamics of this wake. The spanwise compression (figure 16a) is attributed to the mutual induction of opposite-signed streamwise vortices forming pairs at the top and bottom of the wake. The transverse expansion is driven by the self-induction of the curved tips of the horseshoes.

The streamwise variation in the circulation of the streamwise vortices is quantified by measuring the circulations within a vorticity isocontour of 0.06 s^{-1} , as described in §2.2. Figure 21 shows the non-dimensional circulation values of the top legs of horseshoes 1 and 2 as a function of streamwise position. (If the velocity magnitude at a point near the edge of the panel is V_e , then the rate at which the circulation is shed $\sim V_e^2$. We might therefore expect that the circulation of a shed vortex $\sim V_e^2 f^{-1}$. Here we use the approximation that $V_e \sim fC$ and non-dimensionalize the vortex circulations by fC^2 .) In both horseshoes, an increase in streamwise circulation with downstream distance is noted, followed by a decrease as the transverse plane enters the core of the spanwise tip and streamwise vorticity is tilted vertically. Measurements on horseshoe 2 at transverse planes downstream of the trailing edge indicate a linear variation in circulation with a slope of 3.8 mm s^{-1} between the trailing edge and the tip of the structure. The ordinate parameter Γ/fC^2 neglects the contribution of U to the circulation. Although the peak values for $St = 0.43$ and 0.64 are similar, the maximum value at $St = 0.23$ is less since U is of increased importance relative to the transverse velocity of the panel at lower St .

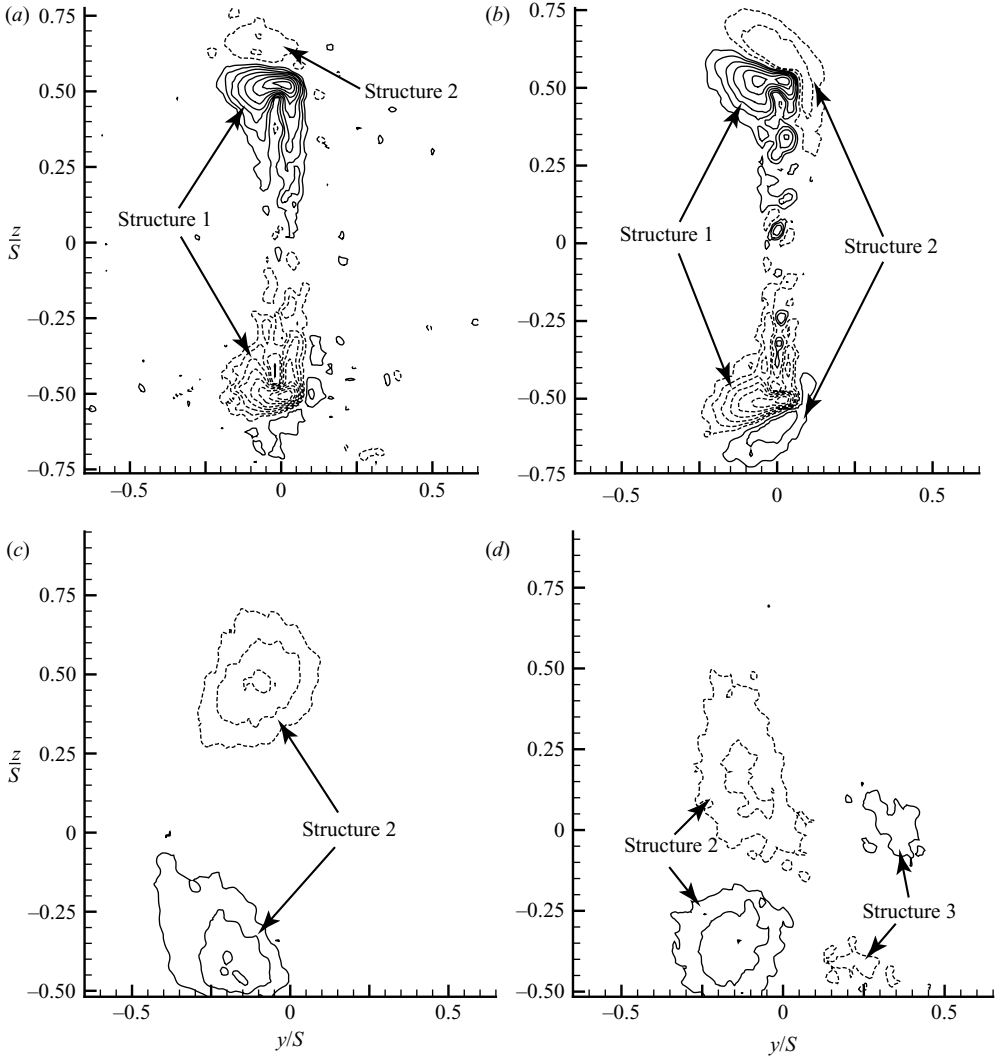


FIGURE 20. Vorticity contours in transverse planes for $St=0.23$, $Re_c=640$. (a) $x/C=-0.25$, (b) 0.017, (c) 0.17, (d) 0.33. Note the vertical shift in field of view at $x/C=0.17$. Contour levels are at $\pm(0.17n)^2 s^{-1}$, $n=2, 3, 4, \dots, 10$. Dashed lines denote negative values.

5.2. The vortex structure at $St=0.43$, $AR=0.54$, $A/S=0.31$

Multiple planes within the wake at $St=0.43$ were visualized using the rotating drum apparatus described in §2.2 in the same manner as implemented by Buchholz & Smits (2006) for the $St=0.23$ case. Figure 22 is composed of 12 planar dye patterns viewed looking upstream, with their streamwise locations superimposed on the central top-view image. The phase angle is $\phi=0^\circ$ again. In the following discussion, structures shed in each half-cycle will be addressed using the same numbering protocol as for $St=0.23$ in §5.1.

Plane *a* is located at $x/C=-0.250$. The trailing edge of the panel coincides with plane *b*. With the panel moving left to right in the transverse planes, vortices are shed from the top and bottom edges of the panel (structure 1) which form counter-rotating pairs with the vortices shed in the previous half-cycle (structure 2), as observed at

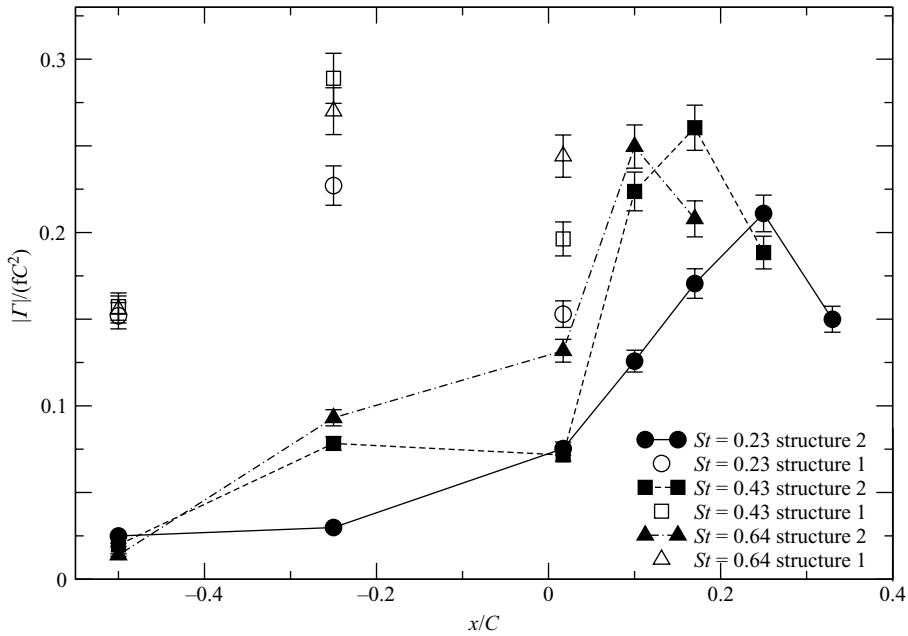


FIGURE 21. Non-dimensional circulation magnitudes of the streamwise legs of the two most recently created horseshoes at various streamwise locations for $St = 0.23, 0.43$ and 0.64 .

$St = 0.23$. However, in this case, a third vortex is visible in these planes, which contains vorticity of the same sign as structure 1 and is part of structure 3 created a full cycle earlier. Its inboard spanwise position is due to induction by the preceding vortex and interaction with its virtual image mirrored by the face of the panel. The greater degree of overlap between structures in this case is due to the greater reduced frequency, $k = fC/U = C/\lambda = 2.6$, compared to 1.4 at $St = 0.23$. Here, λ is an estimate of the streamwise separation between consecutive structures, assuming that they convect at speed U . Structure 1 is terminated by the spanwise tip between planes b and c and a pattern typical of $St = 0.23$ is observed in plane d where an opposite-sign interaction occurs between structures 2 and 3.

However, in planes e to g , the dye patterns become more complicated. In addition to the counter-rotating pairs on the left- and right-hand sides of the wake, an additional vortex pair appears on the right-hand side of the wake near the symmetry plane, evidently emerging from structure 2. In subsequent planes, this pair gradually merges with the vortices of structure 3 which are drawn in from the spanwise edges of the wake. It is simply a branch of structure 3. Just downstream of the tip of structure 2 (plane i), the merge is essentially complete and the pattern again resembles the wake at $St = 0.23$. The emergence of a new vortex pair and subsequent merging with structure 4 is repeated in planes j to l . It is proposed here that these vortex pairs distinguishing the $St = 0.43$ wake from the $St = 0.23$ wake are formed by the reorganization of shear-layer vorticity present at $St = 0.23$ into a discrete spanwise vortex.

Isocontours of streamwise vorticity are presented in figure 23 at four streamwise locations in the wake. Figure 23(a), located at $x/C = -0.25$, is coincident with plane a of figure 22. Although the weak level of vorticity in structure 1 is comparable to the noise in the data, its presence is evident. Structures 1 and 2 are also clearly present

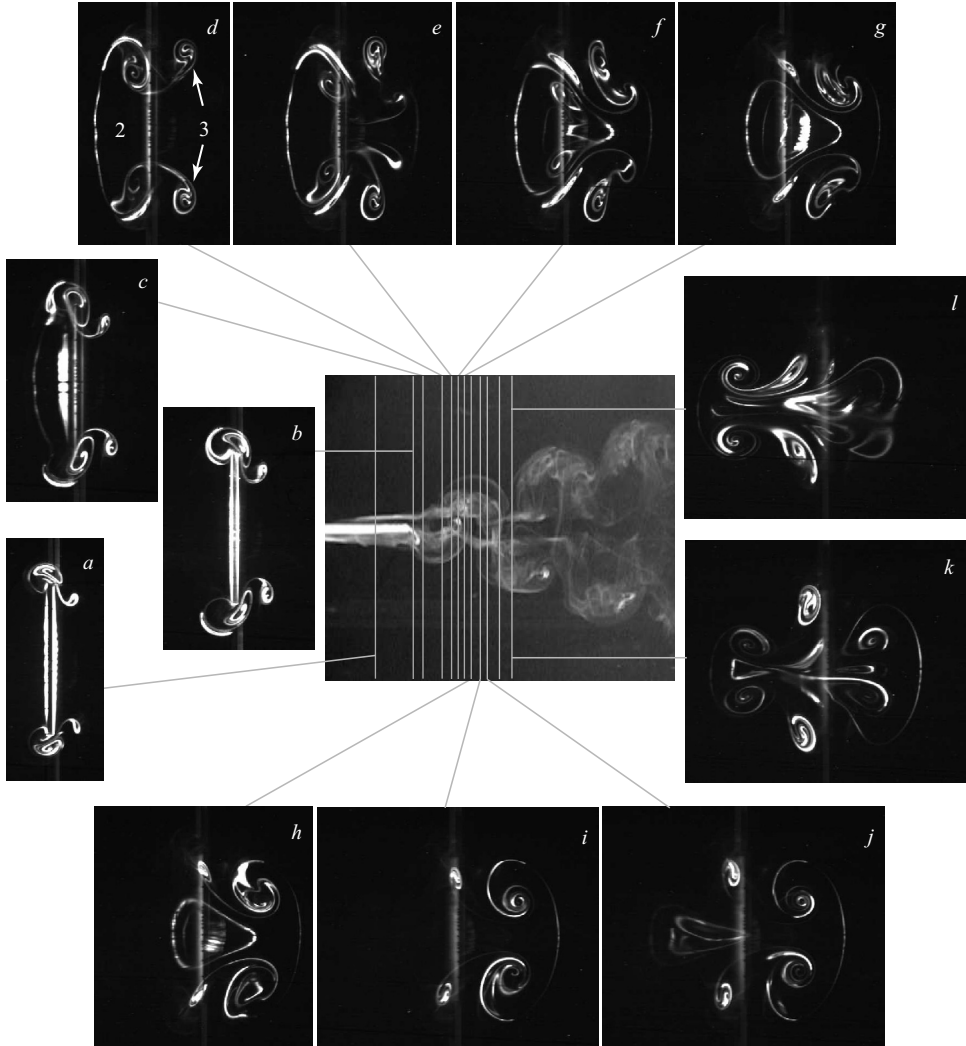


FIGURE 22. Dye visualization of transverse planes for $St=0.43$, $Re_C=640$ superimposed on a top view image for $\phi \approx 0$. Image planes a to l correspond to $x/C = -0.250, 0, 0.063, 0.188, 0.250, 0.292, 0.333, 0.35, 0.438, 0.479, 0.563$ and 0.646 .

in approximately the same positions as the dye visualization indicates. Figure 23(b) lies between planes c and d of figure 22. Vorticity contours reveal structures 2 (left) and 3 (right) as the flow visualization also indicates. (There is a change in the field of view between figures 23(a) and 23(b) which obscures the lower half of the wake from figure 23(b) on. Statements made about these figures are based upon observations of the top half of the wake.) In figure 23(c) ($x/C=0.17$), the second branch of structure 3 is visible as a second local vorticity peak near the symmetry line. While this is also qualitatively consistent, this stage of development is not observed in the dye visualization until approximately $x/C=0.250$ (plane e). This departure is probably caused by slight differences in free-stream speed between the flow visualization and DPIV data. Because the experimental configurations for the acquisition of dye visualization and DPIV data are substantially different, the two

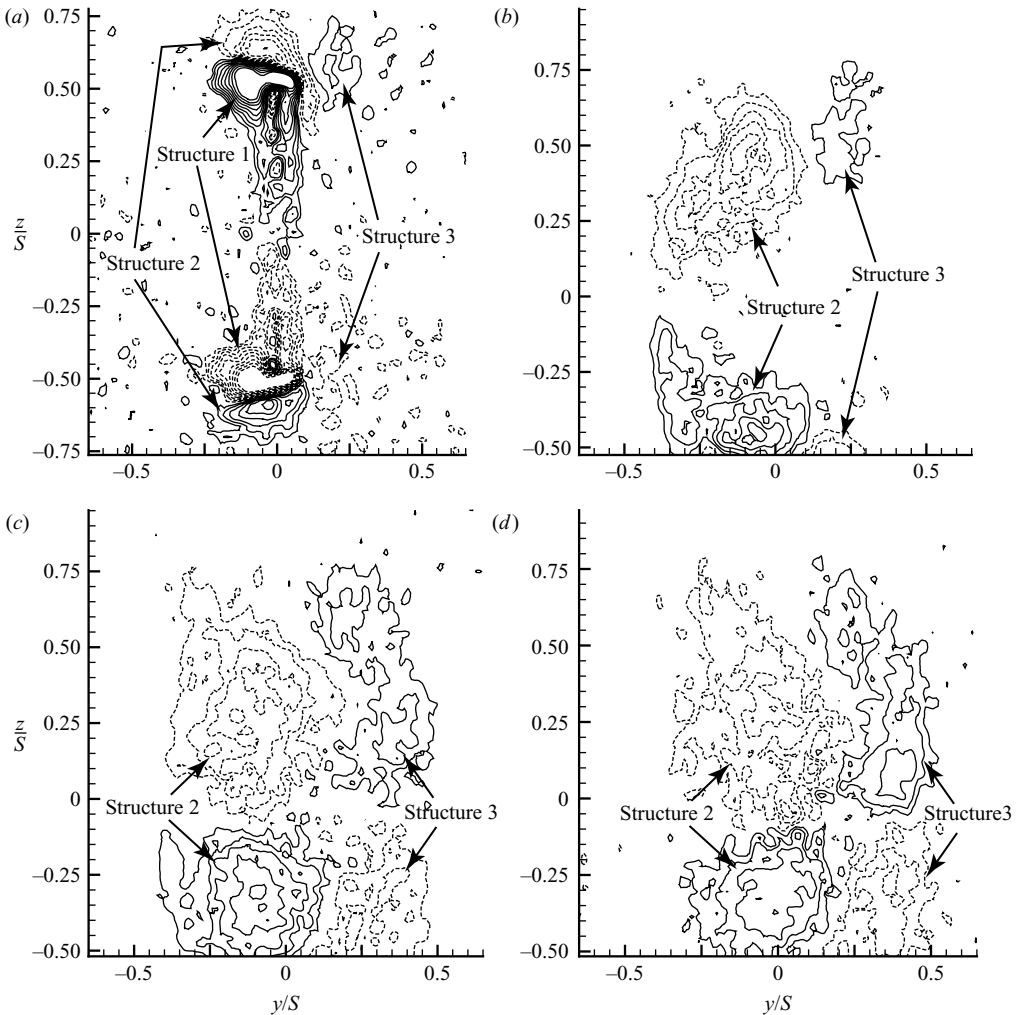


FIGURE 23. Vorticity contours looking upstream for $St=0.43$, $Re_C=640$. Contour levels are at $\pm(0.17n)^2 \text{ s}^{-1}$, $n=2, 3, 4, \dots, 10$. (a) $x=-0.25C$, (b) $0.10C$, (c) $0.17C$, (d) $0.25C$. Dashed lines denote negative values.

data sets were acquired on different days. Finally, in figure 23(d) the outer branch of structure 3 is drawn into the inner branch. This distribution of vorticity, located at $x/C=0.250$ has a similar appearance to the dye patterns in planes *f* and *g* of figure 22 which are at $x/C=0.292$ and 0.333 , respectively.

Figure 21 shows a linear increase in circulation with downstream distance for $St=0.23$. However, for $St=0.43$, there is a sharp increase in the circulation of structure 2 between $x/C=0.017$ and 0.10 of approximately $250 \text{ mm}^2 \text{ s}^{-1}$ ($\Delta\Gamma/fC^2=0.152$). From figure 17(b) it is apparent that these planes approximately bracket the first of the two spanwise vortices shed at the trailing edge at $\phi=0^\circ$. The circulation measured about this spanwise vortex is approximately $270 \text{ mm}^2 \text{ s}^{-1}$ which is similar to the local increase in streamwise circulation shown in figure 21. These measurements are consistent with the presence of a discrete bifurcation in the streamwise vortices that was observed qualitatively in the flow visualization and

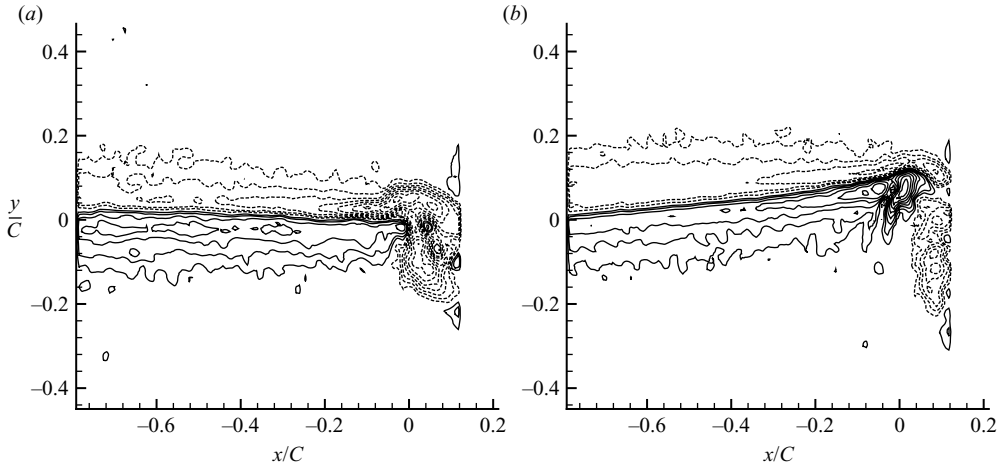


FIGURE 24. Vorticity contours on the panel for $St=0.43$, $Re_c=640$. Contour levels are at $\pm(0.17n)^2 s^{-1}$, $n=2, 3, 4, \dots, 10$. (a) $\phi=0^\circ$, (b) 90° . Dashed lines denote negative values.

PIV data of figures 22 and 23. Furthermore, the combination of the streamwise and spanwise circulation measurements points to a distinct region of spanwise vorticity, shed by the trailing edge as the connecting element of the branches emerging from the top and bottom legs of horseshoe 2.

Contours of spanwise vorticity on the symmetry plane are presented in figure 24 in the vicinity of the panel for $\phi=0^\circ$ and 90° . Figure 24(a) is taken at the same phase as figure 17(b) and there is some overlap between the fields of view in the two images. As the vorticity is shed from the trailing edge at $\phi=0^\circ$, a region of elevated vorticity is generated on the trailing face (the bottom in the figure) of the panel. This distribution convects towards the trailing edge as the panel approaches its maximum excursion in figure 24(b) and two intense peaks of vorticity are formed and shed in the following half-cycle as shown in figure 24(a).

Based on the circulation data presented above, it is proposed that the first spanwise vortex to be shed in figure 17(b) is part of a closed loop connected to a spanwise vortex shed in the preceding half-cycle, and the second spanwise vortex forms a closed loop with a portion of the elevated vorticity observed on the opposite face, upstream on the panel, as drawn in figure 25(a). The resulting structure is a horseshoe with a branch that forms a closed vortex ring connected to its tip, forming the wake shown in figure 25. Despite the markedly different dye pattern formed compared with the $St=0.23$ case, it is entirely consistent with the basic horseshoe structure presented in figure 19(a). Whereas at $St=0.23$, the streamwise legs of the horseshoes are bridged by a relatively uniform shear layer, resulting in a constant rate of increase in their strength with streamwise distance, a portion of the corresponding spanwise vorticity at $St=0.43$ is organized into a localized vortex before being shed adjacent to the tip of the following horseshoe. It is clear that not all of the spanwise vorticity connects to the localized vortex because the streamwise vortex continues upstream of the closed loop.

5.3. The vortex structure at $St=0.64$, $AR=0.54$, $A/S=0.31$

The main difference between the wakes at $St=0.64$ and $St=0.43$ is the additional train of dye patterns, visible in figure 18(a). The underlying structure at $St=0.64$ is qualitatively similar to that at $St=0.43$, which can be verified by a comparison

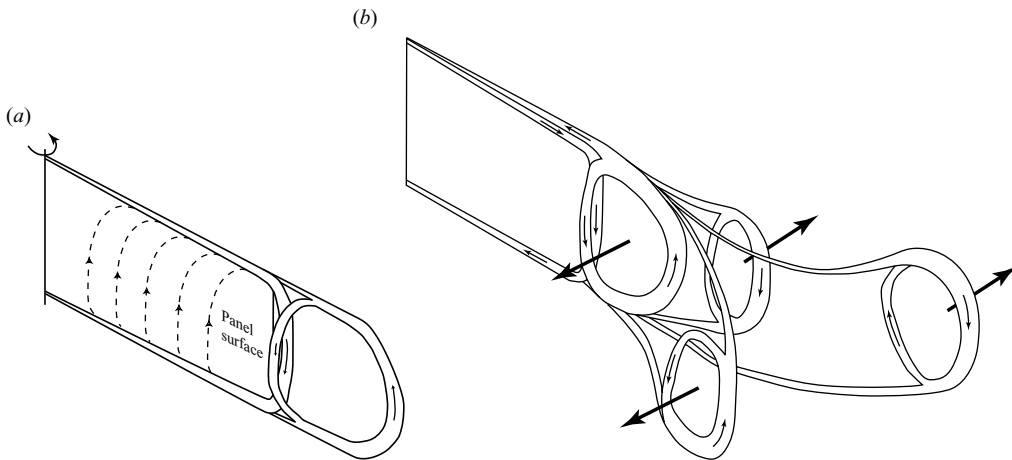


FIGURE 25. (a) A constituent structure at $St = 0.43$, $Re_C = 640$ from which the wake is formed, interacting with the preceding structure. The topology of this structure is the same as at $St = 0.23$ (figure 19a). (b) The resulting wake.

of figures 17(b) and 18(b). The structures are formed at the top and bottom of the wake and do not appear to be dynamically important because their evolution stops about one period after their formation. It is therefore difficult to capture them using DPIV; however, illumination of the flow with white light while capturing video has revealed a probably robust evolution of these structures from the streamwise legs of the structures shed by the panel.

The origin and evolution of these structures is revealed in figure 26 (p. 349) which contains a sequence of top-view images showing their generation from a perturbation in the streamwise leg of the horseshoe shed in the previous half-cycle. Movie 3 (available with the online version of the paper) illustrates that the initial perturbation is concurrent with the generation of the subsequent structure. In each half-cycle, the formation of a counter-rotating vortex pair can be observed in this view from the perturbation (indicated by the arrows in figures 26a and 26d) which develops just upstream of the trailing edge while the subsequent horseshoe is being generated (i.e. the perturbation develops approximately one half-cycle after the generation of the streamwise vortex, possibly initiated by the shedding of the subsequent structure). Video footage from the side (not shown) reveals rotation about a transverse axis at the top of the structure which, combined with the top-view visualization of figure 26, describes a hairpin vortex developing from the perturbation in the streamwise leg. The secondary structure is shown in figure 27. The orientation of the structures would cause them to convect inward toward the symmetry plane; however, viscous diffusion causes rapid annihilation of the vorticity and the motion dissipates rapidly so the dye patterns stay at the spanwise extrema. These structures appear to be analogous to those observed at moderate Reynolds numbers in figure 14(b). At the higher Reynolds numbers, their evolution is naturally much more complex.

6. Discussion

The geometry and kinematics of the flat-plate propulsor investigated here were designed with the goal of simplifying the parametric description of the problem and the flow field. In designing this propulsor for simplicity, compromises were made which

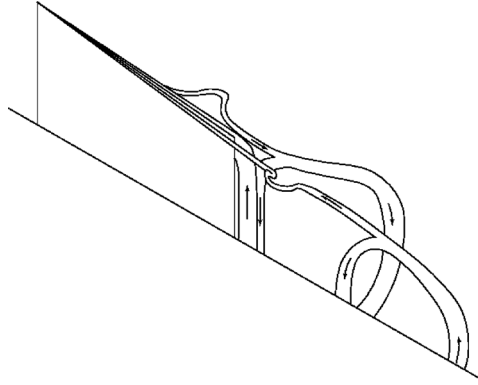


FIGURE 27. Growth of hairpins from the streamwise legs of horseshoe vortices, $St = 0.64$, $Re_C = 640$ at $\phi \approx 270^\circ$, shown in figure 26(d). Only the top half of the wake is shown. The bottom is symmetrical.

cause the device to deviate from the morphology of aquatic animals and from the geometry and kinematics of efficient biomimetic propulsors. Distinguishing features of the present geometry include the absence of flexibility and variation in thickness, the rectangular shape, simple kinematics and the presence of the stationary support fairing upstream of the leading edge of the panel. Furthermore, the detailed wake models proposed in § 5 are obtained for fixed $AR = 0.54$, $A/S = 0.31$ and $Re_C = 640$. Here, we demonstrate that, despite these constraints, the results can be generalized because the wake structure is apparently quite robust with respect to variation in Reynolds number, geometry and kinematics. We also discuss the relationship between wake structure and thrust performance.

6.1. Sensitivity of wake structure to Reynolds number

The low- and moderate-Reynolds-number wakes have many physical similarities. At Strouhal numbers exceeding approximately 0.25, the wakes bifurcate forming oblique vortex pairs. At sufficiently high Strouhal number, this is often accompanied by a spanwise expansion of the wake, whereas within a range of reduced Strouhal numbers, a spanwise compression is observed. For $St \approx 0.2$, the low-Reynolds-number wake and some of the moderate-Reynolds-number wakes exhibit a pattern that, in the symmetry plane, consists of a staggered array of alternating sign vortices.

The low- Strouhal-number behaviour ($St = 0.23$ at $Re_C = 640$) is of particular interest because while, at moderate Reynolds numbers, the highest measured propulsive efficiencies were often commensurate with a simple staggered array of vortices in a reverse Kármán pattern, the orientation of the vorticity at $Re_C = 640$ clearly indicates drag. This Strouhal number is also near the range in which aquatic animals are known to swim (Triantafyllou *et al.* 1991, 1993), forming a reverse Kármán pattern in the symmetry plane (Triantafyllou & Triantafyllou 1995). The significant change in performance between the low- and moderate-Reynolds-number cases is attributed to the relative magnitude of surface pressures from which thrust is generated, to viscous shear stresses which primarily produce drag (note that separated flows may produce small shear stresses that make a positive contribution to the thrust). The low-Reynolds-number wake structure presented in figure 19(b), and the DPIV data presented in figure 20, indicate a mechanism for the spanwise compression based on the interaction of the streamwise components of consecutive horseshoes. However, if the model of figure 19(b) were modified by reversing the signs

of the vorticity to match the orientation of spanwise vorticity observed at moderate-Reynolds-number, the induction of the streamwise vortices would cause spanwise growth where compression is observed. Furthermore, while the transverse growth of the low-Reynolds-number wake is understood as the self-induction of each horseshoe, reversing the signs would drive a transverse compression. The data presented here do not provide a clear explanation of the structure of the wake produced at moderate ($O(10^4)$) Reynolds numbers and low Strouhal numbers (≈ 0.23); however, we may speculate on the structure based on observations made here and in the literature as follows.

At $St=0.23$, $Re_C=640$, the shear layer bridging the legs of a horseshoe structure appears to be stable under these conditions since we do not observe the roll-up of discrete spanwise vortices within the shear layer. At higher Strouhal number, a discrete vortex does form, and it is therefore likely that this also occurs at higher Reynolds number where the shear layer would be thinner. Thus, it is expected that at moderate Reynolds numbers where the near wake has a simple 2-S structure (such as for $AR=0.83$, $A/S=0.31$, $St=0.21$, shown in figure 12*b*), the fundamental constituent of the wake is represented by figure 25, which provides an explanation for the transverse growth and eventual bifurcation of the wake. However, rather than shedding two discrete spanwise vortex pairs as illustrated in figure 17, they coalesce in a synchronization regime analogous to that observed in the flows generated by two-dimensional foils. The hypothesized wake resulting from this development is thus a chain of adjacent vortex rings of alternating sign, as proposed, for example, by Drucker & Lauder (1999) for the propulsion by pectoral fins in bluegill sunfish. In the present case, the convection of these structures is ultimately dominated by their self-induction, and they move transversely, causing the wake eventually to bifurcate. Careful articulation of the foil and the introduction of flexibility would probably delay the bifurcation.

The low-Reynolds-number bifurcating wake model shown in figure 25(*b*) is also consistent with moderate-Reynolds-number observations at higher Strouhal numbers ($St > 0.25$). The wakes within both Reynolds-number ranges bifurcate through the formation of oblique vortex rings, which convect outward in the transverse direction. While the moderate-Reynolds-number bifurcating wakes are generating a mean positive thrust, it has not been possible to measure the small forces applied by the panel at $Re_C=640$. However, variation of the streamwise mean force between thrust and drag, and corresponding changes in efficiency can be, in principle, explained through a variable orientation of the vortex rings.

6.2. Sensitivity of wake structure to geometry and kinematics

The generation of dynamic stall vortices that combine with vorticity shed from the trailing edge has been associated with enhanced thrust production in two-dimensional unsteady propulsors (Anderson *et al.* 1998). Visualizations of the wakes of airfoils and finite wings actuated in pitching and heaving motions have shown dynamic stall vortices to be a robust feature of unsteady propulsion (Freythuth 1988; Anderson *et al.* 1998; von Ellenrieder *et al.* 2003; Guglielmini 2004; Dong *et al.* 2005). Desynchronization of the shedding events such that the leading- and trailing-edge vortices do not coalesce generally occur at Strouhal numbers greater than that at which optimum efficiency is attained, and yield wakes consisting of two or more vortices per half-cycle.

In the present geometry, dynamic stall vortices are not observed; however, it was noted in §5.2 that a concentration of vorticity is generated on the surface of the

panel, growing as it convects down the panel chord, as the DPIV data of figure 24 demonstrate. The lack of a heaving motion and the presence of the fairing upstream of the panel reduce adverse pressure gradients near the leading edge such that large-scale-leading edge separation does not occur. However, this does not appear to change the topology of the vortex structure from a geometry that exhibits dynamic stall.

The behaviour of the wakes of other three-dimensional pitching and heaving foils is largely consistent with the wake models presented in §5. Clark & Smits (2006) propose a vortex skeleton model of the wake produced by an articulated fin of elliptical planform, for $St=0.15$. The wake consists of horseshoe vortices exhibiting streamwise variation in strength, and undergoing opposite-sign interactions, as observed in figure 19(b). Contrary to the flow field of the rectangular pitching panel, this flow does not exhibit spanwise symmetry owing to the monotonic increase in oscillation amplitude with spanwise coordinate. Consequently, the interaction of streamwise vortices shown in the present work were only observed near the tip of the articulated fin.

The wake computed by Guglielmini (2004) for a pitching and heaving wing at $St=0.175$ consisted of a single chain of vortex loops, similar in appearance to the present wake model for $St=0.23$ presented in figure 19(b). At $St=0.35$, the wake bifurcates into two chains of vortex structures which are consistent with the model of figure 25.

The wake of a pitching and heaving ellipsoid of aspect ratio 2.55, computed by Dong *et al.* (2005) was also shown to bifurcate. In their figure 4, vortex ring structures are clearly visible in each branch of the wake produced at $St=0.6$, $Re_C=200$, and connections between the consecutive structures in each branch are also apparent, indicating an asymmetry in the loops that is similar to the present work (figure 25b). Additional branches emerge from each ring, but are truncated by the isosurface threshold. They appear to be connecting the branches of the wake. A similar connection was also suggested by figure 22 (planes *g* and *q*) for the pitching panel wake at $St=0.43$, $Re_C=640$.

The similarities are not limited to oscillating wings. Perry & Chong (1987) proposed a vortex model for a co-flowing jet undergoing harmonic transverse oscillations, applicable to flows where the momentum flux of the jet is greater than that of the free stream (a *jet*) or less than the free stream (a *wake*). Their model bears a strong resemblance to the present model for $St=0.23$, $Re_C=640$ (figure 19b). Govardhan & Williamson (2005) visualized, using DPIV and Taylor's hypothesis, the wake of a transversely vibrating sphere. Connections between the hairpins are not shown, but the structure also bears a strong resemblance to figure 19(b).

6.3. Wake dynamics and performance characteristics

In some cases, the reverse Kármán wake pattern was observed in the near wake for low-aspect-ratio panels in §4 at and near the Strouhal number of peak efficiency. However, three-dimensional vortex interactions elucidated in §5 resulted in the ultimate transverse growth and bifurcation of the wakes, destroying the simple Kármán pattern. Nevertheless, based on the existence of the reverse Kármán pattern under conditions of efficient thrust production, it is proposed that for low-aspect-ratio panels, increased efficiency is produced when two-dimensional vortex interactions (i.e. between spanwise vortices) become more dominant and three-dimensional vortex interactions (i.e. the self-induction of horseshoe vortices and vortex rings) become less dominant.

In §3, the amplitude-to-span ratio A/S was found to be an important parameter in governing the magnitude of the peak efficiency with variation in Strouhal number (figure 6). The Strouhal number at which the peak efficiency occurred also depends on A/S (figure 7).

The width of the near wake, or the transverse distance separating spanwise vorticity shed by the panel, is approximately equal to the peak-to-peak amplitude of the trailing-edge motion. Likewise, the span of the panel determines the initial separation of the streamwise vortices of a horseshoe. Therefore the ratio A/S also determines an aspect ratio of the near wake such that, for low A/S , the interaction between spanwise vortices approaches a two-dimensional wake, and for large A/S , three-dimensional interactions within a single structure dominate, which appear to be inefficient in producing thrust since this results in the formation of transversely moving vortex rings.

Panel aspect ratio was found to be an important parameter governing thrust coefficient (figure 2), and for panel 1 ($AR=0.54$), peak propulsive efficiency was reduced (figure 5). Since forces at large Re_C are governed primarily by pressure forces on the panel, it is conjectured that the reduction in C_T with decreasing AR is due to a reduced net force on the panel surface caused by the spanwise pressure gradients which become less important at larger AR . The spanwise pressure gradients lead to the generation of nominally streamwise vortices which are not effective in producing forward thrust, hence the reduced efficiency. However, as figure 5 shows, panel aspect ratio has a strong influence on peak efficiency only for $AR < 0.83$.

7. Conclusions

The wake structure and thrust performance produced by finite-aspect-ratio panels pitching about their leading edge has been characterized for $Re_C = O(10^4)$. Four aspect ratios were investigated at three pitching amplitudes and a range of Strouhal numbers varying from $O(0.1)$ to $O(1)$. Maximum propulsive efficiencies for each panel at each pitching amplitude were between 9% and 21% which is significantly less than the maximum reported efficiency of 87% for a two-dimensional pitching and heaving airfoil. However, the simplicity of the present geometry and kinematics allowed a simplified parametric investigation of thrust performance and a detailed investigation of the wake structure.

The thrust coefficient was found to be primarily a function of Strouhal number, panel aspect ratio, and Reynolds number, increasing monotonically with each of these parameters. The propulsive efficiency attained a maximum value in the range $0.125 \leq St \leq 0.34$. The ratio A/S was found to be an important parameter governing both the peak efficiency for a given aspect ratio, and the Strouhal number at which it occurs. Surprisingly, panel aspect ratio AR did not strongly influence the propulsive efficiency except for the lowest aspect ratio panel ($AR=0.54$) where propulsive efficiency was significantly lower than for the other aspect ratios. Large A/C was also found to have an adverse effect on efficiency.

For combinations of $AR > 0.54$, sufficiently low A/S , and $Re_C = O(10^4)$, near the optimal Strouhal number, a quasi-two-dimensional reverse Kármán vortex street was observed in the near wake. At higher St the wake rapidly bifurcated, producing two oblique jets, and at lower St , discrete vortices did not form.

A detailed examination of the wake produced by panel 1 ($AR=0.54$) for $A/S=0.31$ and $Re_C=640$ revealed three distinct three-dimensional wake structures with variation in the Strouhal number. For approximately $0.20 < St < 0.25$, the simplest wake

structure was observed. Detailed dye visualization and DPIV revealed the generation of two horseshoe vortices shed per pitching cycle, which interact with neighbouring structures to form a three-dimensional chain of vortex loops. When viewed along a spanwise axis, the wake represents a transversely-growing Kármán vortex street. A critical attribute is that the streamwise legs of the structures increase in circulation toward the tip. This influences the dynamics of the wake in that the interaction between horseshoes is dominated by the most recently created structure. It also implies the existence of spanwise vorticity bridging the legs which is a salient feature of the wakes observed at higher Strouhal numbers and is consistent with the dynamic stall vortex shed by other unsteady propulsors.

For approximately $St > 0.25$, the low-Reynolds-number wake bifurcates into two oblique trains of vortex structures. At $St = 0.43$, $Re_C = 640$, the individual structures are topologically similar to the structures observed at $St = 0.23$ except that a portion of the spanwise shear layer found at $St = 0.23$ is shed from the trailing edge as a discrete spanwise vortex. The resulting fundamental structure is therefore a vortex ring that is partly entrained into the tip of a horseshoe vortex. At $St = 0.64$, the wake contains an additional feature in which streamwise vortices undergo a perturbation near the trailing edge of the panel which leads to the generation of hairpins that convect outward in the spanwise direction. An analogous global wake behaviour was also observed at moderate Reynolds number.

This work was supported in part by the National Institutes of Health CRCNS grant 1RO1NS054271.

REFERENCES

- ANDERSON, J. M., STREITLIEN, K., BARRETT, D. S. & TRIANTAFYLLOU, M. S. 1998 Oscillating foils of high propulsive efficiency. *J. Fluid Mech.* **360**, 41–72.
- BUCHHOLZ, J. H. J. & SMITS, A. J. 2005 Gallery of fluid motion: the wake of a low aspect ratio pitching plate. *Phys. Fluids* **17**, 091102-1
- BUCHHOLZ, J. H. J. & SMITS, A. J. 2006 On the evolution of the wake structure produced by a low-aspect-ratio pitching panel. *J. Fluid Mech.* **546**, 433–443.
- BUCHHOLZ, J. H. J., JIMÉNEZ, J. M., ALLEN, J. J. & SMITS, A. J. 2003 Hydrodynamics of thrust production in a fish-like flapping membrane. In *13th Intl. Symp. on Unmanned Untethered Submersible Technology*. University of New Hampshire, Durham, NH.
- BUCHHOLZ, J. H. J., CLARK, R. P. & SMITS, A. J. 2008 Thrust performance of unsteady propulsors using a novel measurement system, and concurrent wake patterns. *Exps. Fluids* (in press).
- CLARK, R. P. & SMITS, A. J. 2006 Thrust production and wake structure of a batoid-inspired oscillating fin. *J. Fluid Mech.* **562**, 415–429.
- DABIRI, J. O. & GHARIB, M. 2005 Starting flow through nozzles with temporally variable exit diameter. *J. Fluid Mech.* **538**, 111–136.
- DELO, C. J., KELSO, R. M. & SMITS, A. J. 2004 Three-dimensional structure of a low-Reynolds-number turbulent boundary layer. *J. Fluid Mech.* **512**, 47–83.
- DONG, H., MITTAL, R., BOZKURTAS, M. & NAJAR, F. 2005 Wake structure and performance of finite aspect-ratio flapping foils. *AIAA Paper* 2005-0081.
- DRUCKER, E. G. & LAUDER, G. V. 1999 Locomotor forces on a swimming fish: three-dimensional vortex wake dynamics quantified using particle image velocimetry. *J. Exp. Biol.* **202**, 2393–2412.
- VON ELLENRIEDER, K. D., PARKER, K. & SORIA, J. 2003 Flow structures behind a heaving and pitching finite-span wing. *J. Fluid Mech.* **490**, 129–138.
- FREYMUTH, P. 1988 Propulsive vortical signature of plunging and pitching airfoils. *AIAA J.* **27** (9), 1200–1205.

- GHARIB, M., RAMBOD, E. & SHARIFF, K. 1998 A universal time scale for vortex ring formation. *J. Fluid Mech.* **360**, 121–140.
- GOVARDHAN, R. & WILLIAMSON, C. H. K. 2005 Vortex-induced vibrations of a sphere. *J. Fluid Mech.* **531**, 11–47.
- GUGLIELMINI, L. 2004 Modeling of thrust generating foils. PhD thesis, University of Genoa.
- JIMÉNEZ, J. M. 2002 Low Reynolds number studies in the wake of a submarine model using particle image velocimetry. Master's thesis, Princeton University.
- JIMÉNEZ, J. M., BUCHHOLZ, J. H. J., STAPLES, A. E., ALLEN, J. J. & SMITS, A. J. 2003 Flapping membranes for thrust production. In *IUTAM Symp. on Integrated Modeling of Fully Coupled Fluid–Structure Interactions Using Analysis, Computations, and Experiments, Rutgers University, New Brunswick, NJ* (ed. H. Benaroya & T. Wei), pp. 115–24. Kluwer.
- JONES, K. D., DOHRING, C. M. & PLATZER, M. F. 1998 Experimental and computational investigation of the Knoller–Betz effect. *AIAA J.* **36**, 1240–1246.
- KOOCHESFAHANI, M. M. 1989 Vortical patterns in the wake of an oscillating airfoil. *AIAA J.* **27**, 1200–1205.
- LIGHTHILL, M. J. 1963 Introduction. Boundary layer theory. In *Laminar boundary Layers* (ed. L. Rosenhead), pp. 46–113. Oxford University Press.
- LIM, T. T. 2000 Dye and smoke visualization. In *Flow Visualization: Techniques and Examples* (ed. A. J. Smits & T. T. Lim), pp. 43–72. Imperial College Press, London.
- MILANO, M. & GHARIB, M. 2005 Uncovering the physics of flapping flat plates with artificial evolution. *J. Fluid Mech.* **534**, 403–409.
- OHMI, K., COUTANCEAU, M., LOC, T. P. & DULIEU, A. 1990 Vortex formation around an oscillating and translating airfoil at large incidences. *J. Fluid Mech.* **211**, 37–60.
- OHMI, K., COUTANCEAU, M., DAUBE, O. & LOC, T. P. 1991 Further experiments on vortex formation around an oscillating and translating airfoil at large incidences. *J. Fluid Mech.* **225**, 607–630.
- OSHIMA, Y. & NATSUME, A. 1980 Flow field around an oscillating airfoil. In *Flow Visualization II. Proc. Second Intl Symp. on Flow Visualization, Bochum, W. Germany* (ed. W. Merzkirch). Hemisphere.
- OSHIMA, Y. & OSHIMA, K. 1980 Vortical flow behind an oscillating airfoil. In *Proc. 15th Congress, Intl. Union of Theoretical and Applied Mechanics Amsterdam*: North Holland.
- PERRY, A. E. & CHONG, M. S. 1987 A description of eddying motions and flow patterns using critical-point concepts. *Annu. Rev. Fluid Mech.* **19**, 125–155.
- RAFFEL, M., WILLERT, C. & KOMPENHANS, J. 1998 *Particle Image Velocimetry*. Springer.
- TRIAANTAFYLLOU, G. S., TRIANTAFYLLOU, M. S. & GROSENBAUGH, M. A. 1993 Optimal thrust development in oscillating foils with application to fish propulsion. *J. Fluid Struct.* **7**, 205–224.
- TRIAANTAFYLLOU, M. S. & TRIANTAFYLLOU, G. S. 1995 An efficient swimming machine. *Sci. Am.* **272**, 64–70.
- TRIAANTAFYLLOU, M. S., TRIANTAFYLLOU, G. S. & GOPALKRISHNAN, R. 1991 Wake mechanics for thrust generation in oscillating foils. *Phys. Fluids A* **3** (12), 2835–2837.
- TYTELL, E. D. & LAUDER, G. V. 2004 The hydrodynamics of eel swimming—I. Wake structure. *J. Exp. Biol.* **207**, 1825–1841.
- WILLIAMSON, C. H. K. & ROSHKO, A. 1988 Vortex formation in the wake of an oscillating cylinder. *J. Fluids Struct.* **2**, 355–381.
- WU, J. Z. & WU, J. M. 1996 Vorticity dynamics on boundaries. In *Adv. Appl. Mech.* (ed. J. W. Hutchison & T. Y. Wu), vol. 32, pp. 119–275. Academic.